JOURNAL OF AIRCRAFT
Vol. 47, No. 2, March–April 2010

Analytical Sensitivity Analysis of an Unsteady Vortex-Lattice Method for Flapping-Wing Optimization

Bret K. Stanford* and Philip S. Beran†
U.S. Air Force Research Laboratory, Wright-Patterson Air Force Base, Ohio 45433

DOI: 10.2514/1.46259

This work considers the design optimization of a flapping wing in forward flight with active shape morphing, aimed at maximizing propulsive efficiency under lift and thrust constraints. This is done with an inviscid three-dimensional unsteady vortex-lattice method, for which the moderate level of fidelity is offset by a relatively inexpensive computational cost. The design is performed with a gradient-based optimization, where gradients are computed with an analytical sensitivity analysis. Wake terms provide the only connection between the forces generated at disparate time steps and must be included to compute the derivative of the aerodynamic state at a time step with respect to the wing shape at all previous steps. The cyclic wing morphing, superimposed upon the flapping motions, is defined by a series of spatial and temporal approximations. The generalized coordinates of a finite number of twisting and bending modes are approximated by cubic splines. The amplitudes at the control points provide design variables; increasing the number of variables (providing the wing morphing with a greater degree of spatial and temporal freedom) is seen to provide increasingly superior designs, with little increase in computational cost.

I. Introduction

THE design and optimization of artificial flapping-wing flyers presents considerable difficulties in terms of computational cost: the complex physical phenomena associated with the flight (unsteady low-Reynolds-number vortical flows in conjunction with a nonlinear elastic wing surface undergoing large prescribed rotations and translations) may require a high-fidelity computational tool. Furthermore, the search optimization process typically requires many function evaluations to converge to a relevant optimum. Lower-fidelity numerical tools may help alleviate the burden, either used during the search process in conjunction with a higher-fidelity model [1], used to pare down the field of design variables to those of particular importance, or used alone, if it is thought that the tool is able to adequately capture the physical process that may drive the design.

This work considers an unsteady vortex-lattice method for the design of an avianlike flapping wing in forward flight. The method can compute three-dimensional unsteady flows, but not viscous effects (flow separation, transition, reattachment, etc. [2]) or situations with substantial wing–wake interactions [3]. For largely attached flows, the model should provide a suitable compromise between computation cost and fidelity. Lower-fidelity quasi-steady blade element methods (see Berman and Wang [4], Beran et al. [5], Rakotomamonjy et al. [6], and Madangopal et al. [7] for design optimization studies) allow for low design cost but may not be able to capture relevant aspects of the flow. Conversely, high-fidelity Navier–Stokes flow solvers (see Shyy et al. [8], Ho et al. [9], Tuncer et al. [10], and Soueid et al. [11]) are typically too expensive: most studies are confined to a few design variables, for use with a response-surface-based surrogate optimization.

Literature pertaining to the use of an unsteady vortex-lattice method (extensively detailed by Katz and Plotkin [12]) for flapping flight can be found in the work of Vest and Katz [13] and Fritz and Long [14], who consider simultaneous flapping and twisting (both are needed in conjunction to prevent appreciable flow separation at large angles of attack) in forward flight; the former work shows adequate correspondence with wind-tunnel data. Smith [15] and Zhu [16] discuss the implications of coupling an unsteady vortex-lattice method with an elastic structural flapping model. The latter is able to show the dominance of inertial forces (due to the wing rotation and translation) over aerodynamic forces when flapping in air; the opposite is true in water. A design-oriented study is given by Willis et al. [17], who use a wake-only vortex-lattice method developed by Hall et al. [18]. This method defines a periodic wake geometry traced by the trailing edge of a wing through a single flapping cycle and computes the minimum-power vorticity distribution under force constraints. Willis et al. [17] locate the optimal time-dependent feathering distribution along a flapping wing to align each span station with the local flow (defined by the flapping motions as well as the downwash from the minimum-power wake). Finally, Lebental [19] considers a hybrid method with a vortex lattice along the wing and a vorton approximation in the wake and is thus able to compute hovering motions with strong wing–wake interactions.

Few options exist for optimization with a large number of design variables other than gradient-based methods. Many techniques for computing these design derivatives exist [20], though the current discussion is concerned only with analytical methods: direct and adjoint. The former directly computes the derivative of the system response with respect to the design variables, whereas the latter skips this (typically) superfluous quantity in favor of an adjoint vector, which is independent of the design variables. The use of an adjoint method is generally considered more cost-effective when the number of design variables outnumbers the number of constraints [21]. However, the moderate-fidelity vortex-lattice method is an attractive option in the sense that analytical design sensitivities can be practically computed for a large number of design variables without resorting to adjoint methods, which are notoriously cumbersome for nonlinear unsteady physics [22]. The differential equation for the adjoint vector is provided with terminal conditions and must be integrated in reverse [23]: the system response and the adjoint cannot be computed simultaneously and the storage costs can be large.

For cases such as a vortex-lattice method, in which the Jacobian (i.e., the influence matrix, described below) can be explicitly factorized and stored with little effort, the direct method requires the solution of a single system of equations at each time step with

Presented as Paper 2614 at the AIAA Structures, Structural Dynamics, and Materials Conference, Palm Springs, CA, 4–7 May 2009; received 6 July 2009; revision received 27 October 2009; accepted for publication 27 October 2009.

*National Research Council Postdoctoral Researcher, Air Vehicles Directorate; bret.stanford@wpafb.af.mil.

†Principal Research Aerospace Engineer, Air Vehicles Directorate. Associate Fellow AIAA.

multiple right-hand sides (equal to the number of design variables) [24]. The cost of such an endeavor grows very slowly with the number of design variables. Conversely, for cases in which the Jacobian is never explicitly factorized (high-fidelity Navier–Stokes solvers, for example), the cost grows quickly with the number of design variables and adjoint methods are required [24]. Methods for handling the reverse integration and large storage requirements for gradient-based aerodynamic design are given by numerous authors, including Rumpfkeil and Zingg [25] (two-dimensional flows) and Mavriplis [26] (three-dimensional flows). Many of these issues can be alleviated by casting the problem in a time-periodic form: a frequency-domain framework for an unsteady vortex-lattice method is detailed by Hall [27], and the relatively straightforward and inexpensive computations needed for the adjoint vector of the cyclic formulation (harmonic balance) are given by Thomas et al. [28].

This work is, however, solely concerned with a transient analysis (i.e., system response is computed by time-marching), where sensitivities are computed with a direct method. Analytical sensitivities of a steady vortex-lattice method are described by Chittick and Martins [29] and Stanford and Ifju [30] in the context of coupled aeroelastic systems. Murthy and Kaza [31] provide details as to a semi-analytical method for unsteady panel flows (where some derivatives are computed with a finite difference approximation, rather than analytically). Kolonay et al. [32] compute analytical sensitivities of an unsteady doublet-lattice method in the frequency domain; Li and Livne [33] present similar information with a doublet-point method. To the best of the authors' knowledge, a sensitivity analysis of an unsteady vortex-lattice method with a free deforming wake in the time domain is unavailable in the literature and is the focus of the present work.

The remainder of this work is organized as follows: a general description of the unsteady vortex-lattice method is given, as well as explicit matrix operations needed within each time step. This is followed by a derivation of the sensitivity analysis; specifically, the derivative of a time-averaged force quantity (lift, power, etc.) with respect to the shape of the wing at each time step. Results are then given for an avianlike flapping wing in forward flight, in terms of unsteady force generation, wake patterns, and a verification of the sensitivity analysis. The work concludes with a series of design optimization studies, aimed at maximizing the propulsive efficiency of a flapping wing under thrust and lift constraints, with active shape morphing during the flapping stroke. As the wing morphing is given a greater degree of spatial and temporal freedom (i.e., the number of design variables is increased), the optimizer is seen to provide increasingly superior designs, with little increase in computational cost.

II. Unsteady Vortex-Lattice Method

As noted above, the unsteady vortex-lattice method used here will be unable to handle flapping cases with excessive wing–wake interactions (i.e., where the wing will travel through the wake created during the previous stroke), due to the interconnected wake-ring approximation, as opposed to the discrete vorton wake approximation [19]. This restricts the current work to forward-flight configurations, rather than hovering motions. Vortices are only shed from the trailing edge, and thus leading-edge vortices (which can be important at high angles of attack [34]) cannot be considered. As before, such a mechanism is more important for hovering than forward flight, though its exclusion can be expected to lead to an underprediction of the required power input for high reduced frequencies [35]. Finally, the vortex-lattice method can obviously only capture induced drag due to lift and will generally overpredict the thrust (as both viscous and separation drag are missed). The method should be fairly accurate in cases with moderate-to-high Reynolds numbers, moderate-to-high aspect ratios, low angles of attack, and reduced frequencies. However, it is important to emphasize that from a design/optimization standpoint, the vortex-lattice method can typically be used well outside this stated range of validity. The aerodynamic response will certainly have some bias error from the true response (computed with computational fluid dynamics or an experiment), but the computed gradients (discussed below) are still valuable if they can push the design variables in the correct direction.

At a given point in time, the flapping-wing geometry is defined by four metrics. First, in a fixed body frame, the undeformed wing is defined by $\{x_o\}$, a vector with $3 \cdot (M+1) \cdot (N+1)$ quantities (where M is the number of chordwise panels; N the number of spanwise panels; and x, y, and z coordinates are all of interest, hence the 3). This vector is independent of time and does not consider flapping kinematics or local shape changes, as seen on the left of Fig. 1. Second, the morphed wing geometry is given by $\{x^i\}$ (where the superscript denotes the ith time step), a quantity also measured in the fixed body frame. Active shape morphing can be defined by updating this vector in time. The remaining two metrics are defined in an inertial frame, taking into account wing rotation (due to flapping, for example) and translation (due to forward flight): $\{X_r^i\}$ are the corners of each vortex ring, and $\{X_c^i\}$ are the collocation points of each ring, located at the center of each ring (seen on the right of Fig. 1). These latter two are computed by

$$\{X_r^i\} = [Q_r^i] \cdot \{x^i\} + \{\Delta^i\} \qquad \{X_c^i\} = [Q_c^i] \cdot \{x^i\} + \{\Delta^i\} \tag{1}$$

where $[Q_r^i]$ and $[Q_c^i]$ are sparse matrices that serve two functions: they interpolate the wing geometry $\{x^i\}$ onto the corners of the rings (or their collocation points), and they transform the wing shape from a time-fixed body frame to an inertial frame. This is done with a transformation matrix defined by a set of Euler angles (in this case, only the flapping angle β). Δ represents a rigid-body motion (distance traveled by the forward flight). The geometry of the wake, given by the vector $\{X_{\text{wake}}^i\}$, is defined by the trailing edge of the wing. At a given time step, the row of vortex rings that made up the trailing edge at the previous step is convected into the wake, locating the position in space where the wing used to be.

The basics of the unsteady vortex-lattice method are given by Katz and Plotkin [12], which generally operates as follows: At each time step, the wing geometry is updated as defined above. The vortex rings along the trailing edge of the wing are convected into the wake, and the strength (circulation) of each of these rings is set equal to that computed at the previous time step and held fixed. A system of

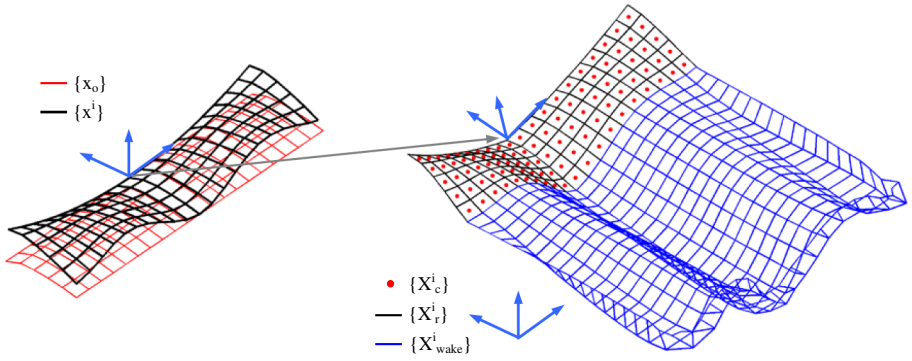

Fig. 1 Body-attached and inertial geometry definitions.

equations is developed and solved for the new circulation distribution throughout the wing: velocities due to wing–wing interactions, wake–wing interactions, freestream velocities, wing rotations (flapping), and wing deformation must all cancel each other in the direction normal to each collocation point. This stipulates that the wing becomes a stream surface of the flow. This wing-circulation distribution can be used to compute the induced velocity at each collocation point (for induced drag computations), pressures, and integrated forces (lift, thrust, etc.). The local streamline at each wake ring can be computed through the wing–wake and wake–wake interactions and subsequently deformed.

Mathematically, the following operations are required at each time step. Based upon prescribed kinematics and/or local wing deformations, the positions of the vortex rings located on the wing are updated with Eq. (1). For the forward flight considered here, $\Delta^i = U_\infty \cdot t$. Next, the row of vortex rings along the trailing edge of the wing is convected into the wake, placed in the area previously occupied by the trailing edge before its translation by Δ^i:

$$\{\bar{X}^i_{\text{wake}}\} = [B^i_1] \cdot \{X^i_r\} + [B^i_2] \cdot \{X^{i-1}_{\text{wake}}\} \tag{2}$$

where $[B^i_1]$ is a very sparse matrix that moves the previous trailing edge into the wake, and $[B^i_2]$ preserves the wake computed at the previous time step as unchanged. As two operations to the wake geometry are required per time step, the barred terms are used as a dummy variable. It should be noted that the wake terms on the left and right sides of Eq. (2) have different sizes, as graphically seen in Fig. 2.

Next, the circulation Γ of the newest wake ring is set equal to the strength of the vortex ring along the trailing edge at the previous time step:

$$\{\Gamma^i_{\text{wake}}\} = [A^i_1] \cdot \{\Gamma^{i-1}_{\text{wake}}\} + [A^i_2] \cdot \{\Gamma^{i-1}_{\text{wing}}\} \tag{3}$$

where $[A^i_1]$ and $[A^i_2]$ serve a similar purpose to that above: the former preserves the strength of the wake computed in the previous time step as unchanged (wake decay algorithms [14] are not included in this work), and the latter sets the strength of the newest wake ring to that of the old trailing edge. While it may seem unusual to cast Eqs. (2) and (3) in matrix form (particularly as all four matrices are extremely sparse), such a formulation is crucial to the sensitivity analysis, as seen in the next section.

A system of equations is built for the no-penetration condition of the wing:

$$[C^i_1] \cdot \{\Gamma^i_{\text{wing}}\} + [C^i_2] \cdot \{\Gamma^i_{\text{wake}}\} = \{L^i\} \tag{4}$$

where $[C^i_1]$ is the wing–wing influence matrix: the mth row and nth column corresponds to the velocity along the outward normal of the mth collocation point due to a unit circulation of the nth ring. Velocities are computed with four applications of the Biot–Savart law for each finite vortex segment of the ring [12]. The wake–wing influence matrix $[C^i_2]$ is computed in a similar manner. Finally, the source vector $\{L^i\}$ is the velocity along the outward normal of each collocation point due to the freestream velocity, wing rotation (flapping), and wing deformation/morphing (the evolution of $\{x^i\}$ in time, but written in the inertial system). As the wake circulation is known from Eq. (3), Eq. (4) can be solved for the current wing circulation. These wing and wake strengths can then be used to compute the induced velocity of each control point:

$$\{w^i\} = [C^i_{w1}] \cdot \{\Gamma^i_{\text{wing}}\} + [C^i_{w2}] \cdot \{\Gamma^i_{\text{wake}}\} \tag{5}$$

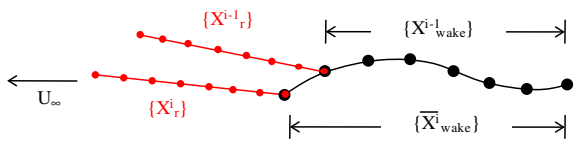

Fig. 2 Wake-shedding procedure of Eq. (2) in two dimensions.

These influence matrices are similar to those found in Eq. (4), but only include the streamwise portions of each vortex ring. The velocity for these terms is not resolved along the outward normal of each panel, but along the local lift vector of each panel (perpendicular to the flow).

The desired objective function (lift, thrust, power, etc.) can now be computed from the wing geometry, circulation distribution, and induced velocity:

$$g^i = f(\{x^i\}, \{X^i_r\}, \{X^i_c\}, \{X^{i-1}_c\}, \{w^i\}, \{\Gamma^i_{\text{wing}}\}, \{\Gamma^{i-1}_{\text{wing}}\}) \tag{6}$$

All time derivatives (wing velocities for the source vector $\{L^i\}$, as well as $\mathrm{d}\Gamma/\mathrm{d}t$ terms for the unsteady Bernoulli equation [12]) are computed with a backward finite difference equation, so information is needed at the previous time step to compute forces within the current time step. The lift and drag of the mth row and nth column of the panel mesh are specifically given as

$$\Delta L^i_{m,n} = \rho \cdot b_{m,n} \cdot \left(\| V^i_{m,n} \| \cdot (\Gamma^i_{m,n} - \Gamma^i_{m-1,n}) + c_{m,n} \cdot \frac{\partial}{\partial t}\left(\frac{\Gamma^i_{m,n} + \Gamma^i_{m-1,n}}{2}\right)\right) \cdot \cos(\alpha_{m,n}) \tag{7}$$

$$\Delta D^i_{m,n} = \rho \cdot b_{m,n} \cdot \left(-w^i_{m,n} \cdot (\Gamma^i_{m,n} - \Gamma^i_{m-1,n}) + c_{m,n} \cdot \frac{\partial}{\partial t}\left(\frac{\Gamma^i_{m,n} + \Gamma^i_{m-1,n}}{2}\right) \cdot \sin(\alpha_{m,n})\right) \tag{8}$$

where ρ is the fluid density, $c_{m,n}$ and $b_{m,n}$ are the chord and span of each panel, $\{V_{m,n}\}$ is the velocity vector of each panel (due to translation, flapping, and wing deformation), and $\alpha_{m,n}$ is the angle of attack of each panel. At the leading edge (where $m = 1$) the $m - 1$ terms are removed from the equations. The angle of attack is found by resolving $\{V^i_{m,n}\}$ along the chord and outward normal of each panel and then using an arctangent function. The quantities in Eqs. (7) and (8) act along the local lift and drag vectors of each panel, which can be transformed into a fixed inertial frame, summed, and then normalized to compute the coefficients of lift and thrust (C_L and C_T) for the entire flapping wing.

Equations (7) and (8) are used to compute the pressure on each panel, which in turn can be used to compute the input power to the system [16]:

$$P^i = \sum_{m=1}^{M} \sum_{n=1}^{N} (b_{m,n} \cdot c_{m,n} \cdot p^i_{m,n} \cdot \{V^i_{m,n}\}^T \cdot \{s^i_{m,n}\}) \tag{9}$$

where $p^i_{m,n}$ and $\{s^i_{m,n}\}$ are the pressure and the outward normal of each panel, respectively. As above, this quantity can be summed over the entire wing and normalized to compute the pressure coefficient C_P. For this work, the inertial power input required to flap the system is neglected (a reasonable assumption for forward flight [2]), as is the work required to morph the wing. Finally, the mean propulsive efficiency of the flapping wing is [13]

$$\eta = \bar{C}_T / \bar{C}_P \tag{10}$$

where the overbar indicates a time-averaged quantity.

Having computed the relevant force metrics, the wake rings must be deformed along the local streamline, in keeping with the force-free assumption [12]. The deformation of the wake is computed as

$$\{\delta^i\} = \Delta t \cdot [D^i_1] \cdot \{\Gamma^i_{\text{wing}}\} + \Delta t \cdot [D^i_2] \cdot \{\Gamma^i_{\text{wake}}\} \tag{11}$$

where $[D^i_1]$ is the wing–wake influence matrix, and $[D^i_2]$ is the wake–wake influence matrix; both matrices are multiplied by a time step to compute a distance metric. These matrices are three times larger than the influence matrices of Eqs. (4) and (5): rather than resolving the Biot–Savart velocities along an outward normal (which does not exist for the corner of each wake ring), all three Cartesian directions are of interest. Based upon the computed deformation, the shape of the wake is updated:

$$\{X^i_{\text{wake}}\} = \{\bar{X}^i_{\text{wake}}\} + [E^i] \cdot \{\delta^i\} \tag{12}$$

where $[E^i]$ reflects the fact that only the portion of the wake not attached to the trailing edge can be moved, as can be seen in Fig. 2. In other words, $\{\delta^i\}$ is only computed for the wake not attached to the trailing edge, and $[E^i]$ pads the vector with extra zeros. Equation (12) represents the second wake operation in this time step, and so the unbarred wake term is reintroduced. The time counter is then updated from i to $i + 1$, and Eqs. (2–12) are repeated.

Significant computational cost savings are available if one only updates the newest wake rows with Eq. (12), rather than the entire wake. The older wake rings typically lie far away from the wing (depending upon the reduced frequency) and have a muted effect upon the wing. As such, a significant portion of $[D^i_1]$ and $[D^i_2]$ can be zero, with a potentially negligible effect upon the computed lift and drag [14]. Furthermore, symmetry about the root is assumed, decreasing the size of all of the influence matrices.

The results of the current vortex-lattice model are compared against Euler computations of Neef and Hummel [36], who study a very similar system to that considered in this work. The flapping wing has a rectangular planform with an aspect ratio of 8, a NACA 0012 airfoil, a flapping amplitude of 15°, and a reduced frequency ($k = \omega \cdot c/2/U_\infty$, where ω is the flapping frequency and c is the wing chord) of 0.1. The flapping motion is sinusoidal, and an out-of-phase wing twist about the leading edge is imposed linearly along the span, culminating in a tip twist amplitude of 4°. More information about active wing twisting and other morphing motions is given below, and details concerning the Euler solver are found in [36]. Comparative results are given in Fig. 3 for a flapping/twisting wing with and without the wing root inclined at a constant angle of attack (pitch) of 4°. As expected, lift is more accurate than thrust, but the agreement in both trends is acceptable. Thrust is particularly overpredicted when the pitch is 4°; this is due to an underprediction in the strength of the tip vortex swirling (i.e., an underprediction of the induced drag), which is shown to be relatively strong in [36]. Wake roll-up is included in the current model (12), but vortex rings are not shed from the wingtips, and so the mechanism is underpredicted. The dissimilarities in the two data sets are not indicative of viscous effects (as both models are inviscid); Fig. 3 merely confirms that the unsteady vortex-lattice method formulated above is able to correctly compute data within its range of validity.

To ascertain errors due to viscous forces, results from the current vortex-lattice model are further compared with experimental data of Heathcote et al. [37], who study a rectangular plunging wing in a water tunnel. The wing has an aspect ratio of 6, a NACA 0012 airfoil, and a chord of 0.1 m. The wing is actuated through a cosine plunging profile with an amplitude of $0.175 \cdot c$, and the Reynolds number is fixed at 30,000. The wing is flexible in the experiment (clamped at the root), and the authors report that the structural response can be adequately represented as a first bending mode with a sinusoidal time history; measured tip displacement and phase lag (behind the root motion) are given on the left of Fig. 4. Aeroelasticity is of no immediate interest to the current work, of course, but the plunging wing can be actively deformed according to the bending profiles of Fig. 4. The unsteady aerodynamic forces generated by the resulting motion can then be computed with unsteady vortex-lattice method for comparison with the experimentally obtained results from the passive deformation. More information about active wing bending is given below, and details concerning the experimental setup are found in [37].

Thrust coefficient as a function of reduced frequency is given on the right of Fig. 4 for both a rigid wing and a dynamically bending wing. The unsteady vortex-lattice method correctly predicts the quadratic growth in thrust with reduced frequency, though the force is again overpredicted. The discrepancy is now due to both tip vortex shedding (as above) and viscous drag via flow separation and skin friction, which can be significant for the low-Reynolds-number flow. As the reduced frequency approaches 0, an experimental C_{D_0} of 0.028 is measured, whereas the inviscid model predicts zero drag. Of paramount importance to the current work, however, is that the model correctly predicts the thrust augmentation due to the dynamic wing bending (the deformation increases the speed of the wingtip and hence the forces); the offset error in thrust prediction is of lower importance from a design/optimization standpoint. Though not shown here, the model is also able to correctly predict the increased power draw and decreased efficiency of the bending wing, as compared with a rigid model.

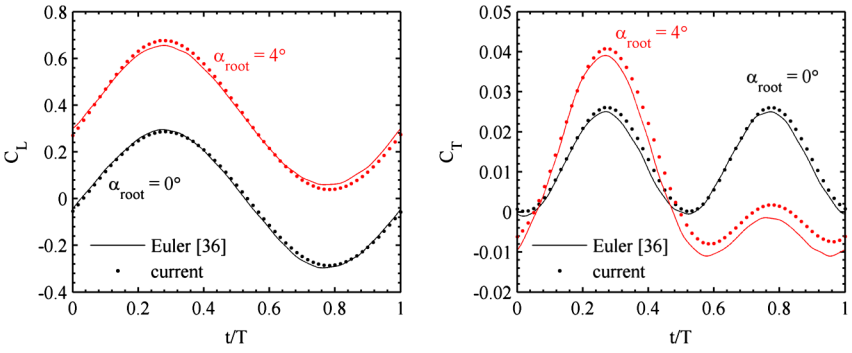

Fig. 3 Comparison of lift and thrust for a flapping/twisting wing with results from [36].

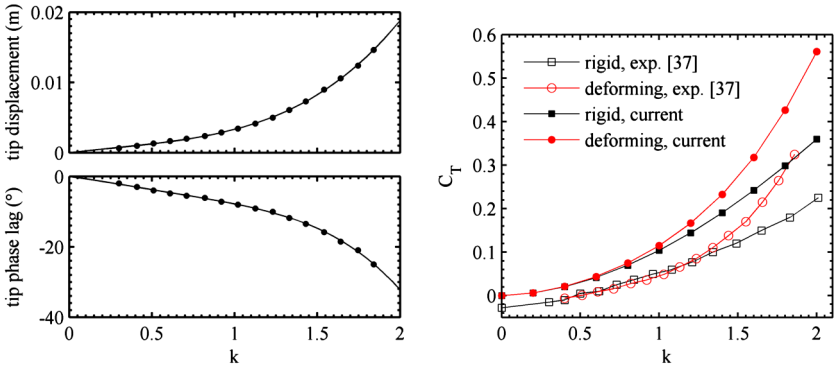

Fig. 4 Comparison of thrust for a plunging/bending wing with results from [37].

III. Analytical Sensitivity Analysis Framework

For this work, the optimization framework will contain objective functions and constraints formulated as a time-averaged (over a complete flapping cycle) force quantity:

$$G = \int_{t_o}^{t_o+T} g \cdot \mathrm{d}t = \sum_{i=I_o}^{I_f} \omega^i \cdot g^i \tag{13}$$

where G is the time-integrated objective function, g^i are force-based metrics measured during the ith time step, and ω^i is a weighting coefficient, reflecting a numerical time-integration scheme. A single period of flapping (T) is assumed to lie between time indices I_o and I_f. Some amount of simulation time is required before the system response becomes time-periodic; these time steps lie before I_o. For this work, design variables are the shape of the wing in the body axis $\{x^i\}$ at each time step. Sensitivities then become

$$\frac{\mathrm{d}G}{\mathrm{d}\{x^j\}} = \sum_{i=\max(j,I_o)}^{I_f} \omega^i \cdot \frac{\mathrm{d}g^i}{\mathrm{d}\{x^j\}} \qquad j = 1, \ldots, I_f \tag{14}$$

The total derivative $\mathrm{d}G/\mathrm{d}\{x^j\}$ is computed with a sum from time step j to the final step I_f, as a change in the wing shape at time step j will only change the aerodynamics in the following time steps. Time steps before I_o are considered in Eq. (14) as well; even though they are not used to explicitly compute G [Eq. (13)], the shape at these steps will still have an implicit influence, particularly for flows with highly unsteady features. Computation of the complete set of derivatives will require the derivative of g^i with respect to the wing shape at every time step before i: using Eq. (14), $\mathrm{d}G/\mathrm{d}\{x^i\}$ will eventually have $3 \cdot (M+1) \cdot (N+1)$ terms (design variables), and there are I_f of these total derivatives (one for each time step).

Facilitating a sensitivity analysis, the following dependencies are observed. From Eq. (4) in the previous section,

$$[C_1^i] = f(\{X_r^i\}, \{X_c^i\}) \qquad [C_2^i] = f(\{X_r^i\}, \{X_c^i\}, \{\bar{X}_{\text{wake}}^i\})$$
$$\{L^i\} = f(\{X_r^i\}, \{X_c^i\}, \{X_c^{i-1}\}) \tag{15}$$

Wing–wing influence matrices depend only upon the shape of the wing, whereas wing–wake influence matrices depend upon the geometry of both the wing and the wake. The source vector $\{L^i\}$ contains velocity terms due to wing flapping and morphing deformation, which are computed with finite differences. As such, the geometry at both the current and the previous time steps are required. From Eq. (5),

$$[C_{w1}^i] = f(\{X_r^i\}, \{X_c^i\}, \{X_c^{i-1}\})$$
$$[C_{w2}^i] = f(\{X_r^i\}, \{X_c^i\}, \{X_c^{i-1}\}, \{\bar{X}_{\text{wake}}^i\}) \tag{16}$$

These influence matrices reflect the induced velocity $\{w^i\}$, which is defined as the flow velocity along the local lift vector of each panel. This vector is defined by the rigid-body motion of the wing (flapping velocity, for example), which, as discussed above, is computed with finite difference terms, necessitating geometry information at the previous time step. From Eq. (11),

$$[D_1^i] = f(\{X_r^i\}, \{\bar{X}_{\text{wake}}^i\}) \qquad [D_2^i] = f(\{\bar{X}_{\text{wake}}^i\}) \tag{17}$$

As above, wing–wake influence matrices depend on the geometry of both the wing and the wake, and wake–wake matrices depend only upon the wake. It is also noted that no relationship is assumed to exist between the wing geometry at disparate time steps: kinematics and morphing wing deformation are both prescribed quantities.

All of the quantities given in Eqs. (15–17) are purely defined by geometry; they are assembled by repeated application of the Biot–Savart law (with the exception of $\{L^i\}$). Therefore, their sensitivities can be computed by taking the derivative of this law. Consider the velocity $\{v\}$ induced at the collocation point of panel L due to a filament of the vortex ring at panel K, seen in Fig. 5. The member of the influence matrix that captures this interaction is given as [12]

$$[C_1^i]_{L,K} = \Gamma_K \cdot \{s\}^T \cdot \left(\frac{\{r_1\} \times \{r_2\}}{4 \cdot \pi \cdot \| \{r_1\} \times \{r_2\} \|} \cdot \left(\{r_o\}^T \cdot \left(\frac{\{r_1\}}{\| \{r_1\} \|} - \frac{\{r_2\}}{\| \{r_2\} \|} \right) \right) + \cdots \right) \tag{18}$$

Equation (18) reflects one of the four filaments in panel K; the influences of all four filaments are required, hence the ellipses. The outward normal $\{s\}$ is completely defined by the four ring coordinates of panel $L(X_{r1-4})$, the influence velocity is defined by the collocation point X_c and the two ring coordinates of the filament at panel K (X_{r5-6}), and so the influence matrix member (L, K) is defined by one collocation point and up to eight ring coordinates. If panel L coincides with panel K, then only four ring coordinates are needed. Using this information, as well as the derivative of Eq. (18), the triply indexed matrices $\partial[C_1^i]/\partial\{X_r^i\}$ and $\partial[C_1^i]/\partial\{X_c^i\}$ can be computed. As a single ring coordinate only affects up to four rows/columns of $[C_1^i]$ and a single collocation coordinate affects only one row/column of $[C_1^i]$, both matrices are sparse. Finally, the chain rule can be used to compute the sensitivity of interest:

$$\frac{\partial[C_1^i]}{\partial\{x^i\}} = \frac{\partial[C_1^i]^T}{\partial\{X_r^i\}} \cdot [Q_r^i] + \frac{\partial[C_1^i]^T}{\partial\{X_c^i\}} \cdot [Q_c^i] \tag{19}$$

Similar methods can be used to compute derivatives of the remaining influence matrices.

The derivative of the objective function at time step i (g^i) with respect to the wing geometry is given by

$$\frac{\mathrm{d}g^i}{\mathrm{d}\{x^j\}} = \begin{cases} \frac{\partial g^i}{\partial\{x^i\}} + \frac{\partial g^i}{\partial\{X_r^i\}}^T \cdot [Q_r^i] + \frac{\partial g^i}{\partial\{X_c^i\}}^T \cdot [Q_c^i] + \frac{\partial g^i}{\partial\{w^i\}} \cdot \frac{\partial\{w^i\}}{\partial\{x^i\}} + \frac{\partial g^i}{\partial\{\Gamma_{\text{wing}}^i\}}^T \cdot \frac{\partial\{\Gamma_{\text{wing}}^i\}}{\partial\{x^i\}}, & j = i \\ \frac{\partial g^i}{\partial\{X_c^{i-1}\}}^T \cdot [Q_c^{i-1}] + \frac{\partial g^i}{\partial\{w^i\}}^T \cdot \frac{\partial\{w^i\}}{\partial\{x^{i-1}\}} + \frac{\partial g^i}{\partial\{\Gamma_{\text{wing}}^i\}}^T \cdot \frac{\partial\{\Gamma_{\text{wing}}^i\}}{\partial\{x^{i-1}\}} + \frac{\partial g^i}{\partial\{\Gamma_{\text{wing}}^{i-1}\}}^T \cdot \frac{\partial\{\Gamma_{\text{wing}}^{i-1}\}}{\partial\{x^{i-1}\}}, & j = i-1 \\ \frac{\partial g^i}{\partial\{w^i\}}^T \cdot \frac{\partial\{w^i\}}{\partial\{x^j\}} + \frac{\partial g^i}{\partial\{\Gamma_{\text{wing}}^i\}}^T \cdot \frac{\partial\{\Gamma_{\text{wing}}^i\}}{\partial\{x^j\}} + \frac{\partial g^i}{\partial\{\Gamma_{\text{wing}}^{i-1}\}}^T \cdot \frac{\partial\{\Gamma_{\text{wing}}^{i-1}\}}{\partial\{x^j\}}, & j < i-1 \end{cases} \tag{20}$$

A piecewise expression is required because an explicit relationship between the geometry at step j and the loads at step i only exist if $j \geq i-1$. When j and i coincide, an explicit term $\partial g^i/\partial\{x^i\}$ exists, as $\{x^i\}$ is used to compute $c_{m,n}$ and $b_{m,n}$ in Eqs. (7–9). Transposed terms in Eq. (20) can be computed directly, using the expressions in Eqs. (7–10), whereas the remaining terms require additional effort.

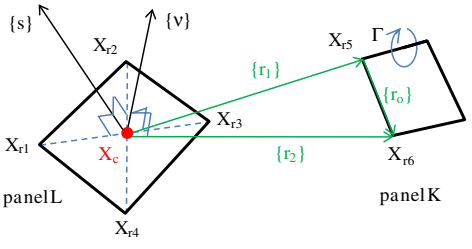

Fig. 5 Geometric quantities needed for the computation of $[C_1^i]_{L,K}$.

As noted above, sensitivity computations of g^i with respect to the geometry at step i and all preceding steps are required to compute $\mathrm{d}G/\mathrm{d}\{x^j\}$ in Eq. (14). As such, at the ith step, it will only be necessary to use the following equations to compute $\partial\Phi^i/\partial\{x^i\}$, $\partial\Phi^i/\partial\{x^{i-1}\}$, $\partial\Phi^i/\partial\{x^{i-2}\}$, etc. (where Φ can be the induced velocity or the wing circulation). These terms can then be inserted into Eq. (20) to compute $\mathrm{d}g^i/\mathrm{d}\{x^j\}$. Additional terms (also required to compute sensitivities of Φ^i) such as $\partial\Phi^{i-1}/\partial\{x^{i-1}\}$ or $\partial\Phi^{i-2}/\partial\{x^{i-4}\}$ (for example) will already be known from similar computations at previous time steps.

Derivatives of the wing circulation with respect to the wing shape are given by derivatives of Eq. (4):

$$\frac{\partial\{\Gamma^i_{\text{wing}}\}}{\partial\{x^j\}} = \begin{cases} [C_1^i]^{-1}\cdot\left(\frac{\partial\{L^i\}}{\partial\{x^i\}} - \frac{\partial[C_1^i]}{\partial\{x^i\}}\cdot\{\Gamma^i_{\text{wing}}\} - \frac{\partial[C_2^i]}{\partial\{x^i\}}\cdot\{\Gamma^i_{\text{wake}}\}\right), & j = i \\ [C_1^i]^{-1}\cdot\left(\frac{\partial\{L^i\}}{\partial\{x^{i-1}\}} - \frac{\partial[C_2^i]}{\partial\{x^{i-1}\}}\cdot\{\Gamma^i_{\text{wake}}\} - [C_2^i]\cdot\frac{\partial\{\Gamma^i_{\text{wake}}\}}{\partial\{x^{i-1}\}}\right), & j = i-1 \\ [C_1^i]^{-1}\cdot\left(-\frac{\partial[C_2^i]}{\partial\{x^j\}}\cdot\{\Gamma^i_{\text{wake}}\} - [C_2^i]\cdot\frac{\partial\{\Gamma^i_{\text{wake}}\}}{\partial\{x^j\}}\right), & j < i-1 \end{cases} \tag{21}$$

As above, piecewise expressions are required because $\{L^i\}$ is only a function of $\{x^i\}$ and $\{x^{i-1}\}$ [Eq. (15)], and the wake circulation at step i is not a function of the geometry at step i [Eq. (3)]. Each of the piecewise expressions requires the solution to a system of equations with multiple right-hand sides (one for each design variable, the size

Equation (22) is the derivative of Eq. (3); the wing circulation sensitivity $\partial\{\Gamma^{i-1}_{\text{wing}}\}/\partial\{x^j\}$ will be known from computations pertaining to g^{i-1}, but would be unavailable had an adjoint method been used. The derivative of the wake–wing influence matrix needed above is computed with the chain rule:

$$\frac{\partial[C_2^i]}{\partial\{x^j\}} = \begin{cases} \frac{\partial[C_2^i]^T}{\partial\{X_r^i\}}\cdot[Q_r^i] + \frac{\partial[C_2^i]^T}{\partial\{X_c^i\}}\cdot[Q_c^i] + \frac{\partial[C_2^i]}{\partial\{\bar{X}^i_{\text{wake}}\}}^T\cdot\frac{\partial\{\bar{X}^i_{\text{wake}}\}}{\partial\{x^i\}}, & j = i \\ \frac{\partial[C_2^i]}{\partial\{\bar{X}^i_{\text{wake}}\}}^T\cdot\frac{\partial\{\bar{X}^i_{\text{wake}}\}}{\partial\{x^j\}} & j < i \end{cases} \tag{23}$$

Sensitivity of the barred wake geometry terms with respect to the wing geometry requires derivatives of Eq. (2):

$$\frac{\partial\{\bar{X}^i_{\text{wake}}\}}{\partial\{x^j\}} = \begin{cases} [B_1^i]\cdot[Q_r^i], & j = i \\ [B_2^i]\cdot\frac{\partial\{X^{i-1}_{\text{wake}}\}}{\partial\{x^j\}}, & j < i \end{cases} \tag{24}$$

Sensitivity of the unbarred wake terms requires derivatives of Eq. (12):

$$\frac{\partial\{X^i_{\text{wake}}\}}{\partial\{x^j\}} = \frac{\partial\{\bar{X}^i_{\text{wake}}\}}{\partial\{x^j\}} + [E^i]\cdot\frac{\partial\{\delta^i\}}{\partial\{x^j\}} \tag{25}$$

The sensitivity of the wake deformation is given by derivatives of Eq. (11):

$$\frac{\partial\{\delta^i\}}{\partial\{x^j\}} = \begin{cases} \Delta t\cdot(\frac{\partial[D_1^i]}{\partial\{x^i\}}\cdot\{\Gamma^i_{\text{wing}}\} + [D_1^i]\cdot\frac{\partial\{\Gamma^i_{\text{wing}}\}}{\partial\{x^i\}} + \frac{\partial[D_2^i]}{\partial\{x^i\}}\cdot\{\Gamma^i_{\text{wake}}\}), & j = i \\ \Delta t\cdot(\frac{\partial[D_1^i]}{\partial\{x^j\}}\cdot\{\Gamma^i_{\text{wing}}\} + [D_1^i]\cdot\frac{\partial\{\Gamma^i_{\text{wing}}\}}{\partial\{x^j\}} + \frac{\partial[D_2^i]}{\partial\{x^j\}}\cdot\{\Gamma^i_{\text{wake}}\} + [D_2^i]\cdot\frac{\partial\{\Gamma^i_{\text{wake}}\}}{\partial\{x^j\}}), & j < i \end{cases} \tag{26}$$

At this point, all of the information needed to compute the system response derivative in Eq. (21) (for given time steps i and j) is available. The derivative of the induced velocities is also required for Eq. (20). Differentiating Eq. (5),

$$\frac{\partial\{w^i\}}{\partial\{x^j\}} = \begin{cases} \frac{\partial[C^i_{w1}]}{\partial\{x^i\}}\cdot\{\Gamma^i_{\text{wing}}\} + [C^i_{w1}]\cdot\frac{\partial\{\Gamma^i_{\text{wing}}\}}{\partial\{x^i\}} + \frac{\partial[C^i_{w2}]}{\partial\{x^i\}}\cdot\{\Gamma^i_{\text{wake}}\}, & j = i \\ \frac{\partial[C^i_{w1}]}{\partial\{x^{i-1}\}}\cdot\{\Gamma^i_{\text{wing}}\} + [C^i_{w1}]\cdot\frac{\partial\{\Gamma^i_{\text{wing}}\}}{\partial\{x^{i-1}\}} + \frac{\partial[C^i_{w2}]}{\partial\{x^{i-1}\}}\cdot\{\Gamma^i_{\text{wake}}\} + [C^i_{w2}]\cdot\frac{\partial\{\Gamma^i_{\text{wake}}\}}{\partial\{x^{i-1}\}}, & j = i-1 \\ [C^i_{w1}]\cdot\frac{\partial\{\Gamma^i_{\text{wing}}\}}{\partial\{x^j\}} + \frac{\partial[C^i_{w2}]}{\partial\{x^j\}}\cdot\{\Gamma^i_{\text{wake}}\} + [C^i_{w2}]\cdot\frac{\partial\{\Gamma^i_{\text{wake}}\}}{\partial\{x^j\}}, & j < i-1 \end{cases} \tag{27}$$

of $\{x^i\}$): a hallmark of the direct method of analytical differentiation of discrete systems [24]. As a given influence matrix must be inverted more than once (a single time for the original vortex-lattice solver and many times for the sensitivity analysis, particularly for a matrix that resides toward the beginning of the flapping cycle), each $[C_1^i]$ can be factorized and stored in memory.

As the size of the design variable vector $\{x^i\}$ is very large, adjoint methods are typically preferable, which require a computational cost that is nearly independent of the number of variables [21]. However, in addition to complexities associated with adjoint methods for transient problems discussed above, these methods skip the computation of the derivative of the system response with respect to the design variable (in this case, $\partial\{\Gamma^i_{\text{wing}}\}/\partial\{x^j\}$) altogether. These terms, however, are needed for additional computations concerning the wake, as seen below:

$$\frac{\partial\{\Gamma^i_{\text{wake}}\}}{\partial\{x^j\}} = \begin{cases} [A_2^i]\cdot\frac{\partial\{\Gamma^{i-1}_{\text{wing}}\}}{\partial\{x^{i-1}\}}, & j = i-1 \\ [A_1^i]\cdot\frac{\partial\{\Gamma^{i-1}_{\text{wake}}\}}{\partial\{x^j\}} + [A_2^i]\cdot\frac{\partial\{\Gamma^{i-1}_{\text{wing}}\}}{\partial\{x^j\}}, & j < i-1 \end{cases} \tag{22}$$

All circulation derivative terms needed for Eq. (27) are previously computed in Eqs. (21) and (22). Additionally, the derivative of the wake–wing influence matrices for the induced velocities [Eq. (16)] needed above is

$$\frac{\partial[C^i_{w2}]}{\partial\{x^j\}} = \begin{cases} \frac{\partial[C^i_{w2}]^T}{\partial\{X_r^i\}}\cdot[Q_r^i] + \frac{\partial[C^i_{w2}]^T}{\partial\{X_c^i\}}\cdot[Q_c^i] + \frac{\partial[C^i_{w2}]}{\partial\{\bar{X}^i_{\text{wake}}\}}^T\cdot\frac{\partial\{\bar{X}^i_{\text{wake}}\}}{\partial\{x^i\}}, & j = i \\ \frac{\partial[C^i_{w2}]^T}{\partial\{X_c^{i-1}\}}\cdot[Q_c^{i-1}] + \frac{\partial[C^i_{w2}]}{\partial\{X^i_{\text{wake}}\}}^T\cdot\frac{\partial\{\bar{X}^i_{\text{wake}}\}}{\partial\{x^{i-1}\}}, & j = i-1 \\ \frac{\partial[C^i_{w2}]}{\partial\{\bar{X}^i_{\text{wake}}\}}^T\cdot\frac{\partial\{\bar{X}^i_{\text{wake}}\}}{\partial\{x^j\}}, & j < i \end{cases} \tag{28}$$

Upon completion of these steps, the following terms are known: $\partial\{\Gamma^i_{\text{wing}}\}/\partial\{x^j\}$, $\partial\{\Gamma^{i-1}_{\text{wing}}\}/\partial\{x^j\}$, and $\partial\{w^i\}/\partial\{x^j\}$, which can be used to compute $\mathrm{d}g^i/\mathrm{d}\{x^j\}$ in Eq. (20). This entire process is then repeated for $j-1$ and $j-2,\ldots,1$ to compute

$$\mathrm{d}g^i/\mathrm{d}\{x^{j-1}\}, \qquad \mathrm{d}g^i/\mathrm{d}\{x^{j-2}\} \quad \cdots \quad \mathrm{d}g^i/\mathrm{d}\{x^1\}$$

Then i can be increased by one, and the entire (reverse time-stepping) process is repeated until i is equal to I_f. At this point, the global derivative $\mathrm{d}G/\mathrm{d}\{x\}$ can be assembled with Eq. (14).

As discussed above, the derivative $\mathrm{d}G/\mathrm{d}\{x^i\}$ contains $3 \cdot (M+1) \cdot (N+1)$ terms, and there are I_f of these total derivatives (one for each time step). Providing an optimizer with $3 \cdot (M+1) \cdot (N+1) \cdot I_f$ design variables to optimize, say, the propulsive efficiency is infeasible; both spatial and temporal constraints need to be imposed upon the wing morphing. For example, peak deformation, relative deformation (i.e., wing strains and curvatures), and wing accelerations all need to be limited. Spatially, this can be done by distilling the shape vector $\{x^i\}$ (which contains the x, y, and z coordinates of each node along the wing) into global mode shapes. Four are considered in this work, seen in Fig. 6: first and second twisting (θ_1, θ_2) and first and second bending (δ_1, δ_2). These shapes are computed as

$$\{x^i\} = -\{x_o\} + \{x_o\} \cdot \cos(\theta_1^i \cdot 2 \cdot \{y_o\}/b) + \{x_o\} \cdot \cos(\theta_2^i \cdot (-192 \cdot (\{y_o\}/b)^4 + 224 \cdot (\{y_o\}/b)^3 - 60 \cdot (\{y_o\}/b)^2)) \tag{29}$$

$$\{y^i\} = \{y_o\} + f^i \cdot (\{y_o\}/b)^2 \tag{30}$$

$$\{z^i\} = \{z_o\} - \{x_o\} \cdot \sin(\theta_1^i \cdot 2 \cdot \{y_o\}/b) - \{x_o\} \cdot \sin(\theta_2^i \cdot (-192 \cdot (\{y_o\}/b)^4 + 224 \cdot (\{y_o\}/b)^3 - 60 \cdot (\{y_o\}/b)^2)) + \delta_1 \cdot (\{y_o\}/b)^2 + \delta_2 \cdot (-192 \cdot (\{y_o\}/b)^4 + 224 \cdot (\{y_o\}/b)^3 - 60 \cdot (\{y_o\}/b)^2) \tag{31}$$

where f^i is the spanwise foreshortening of the wing, computed from δ_1 and δ_2 so as to preserve the length of the wing from root to tip, and b is the wing span. The first twisting mode (θ_1) is identical to that used in Fig. 3, as described in [36].

The size of the total derivative $\mathrm{d}G/\mathrm{d}\{x\}$ has now been distilled from $3 \cdot (M+1) \cdot (N+1) \cdot I_f$ to $4 \cdot I_f$. Temporally, the design variables can further be compressed by assuming that the generalized coordinates (amplitudes) of each mode are determined by a periodic cubic spline, or by a sinusoid. For the former, the motion is controlled by 7 kt equally spaced over the flapping cycle $(t/T = 0, 1/7, \ldots, 6/7$; the value at $t/T = 1$ is assumed to be the same as at $t/T = 0$ for time periodicity), and the final number of design variables is 28. For the latter, the amplitude and phase control the generalized amplitude, and the final number of design variables is eight. The sensitivities computed in Eq. (14) must also be distilled using the chain rule. For the first twisting mode, for example,

$$\{\theta_1\} = \left\{ \theta_1^1 \quad \theta_1^2 \quad \cdots \quad \theta_1^{I_f} \right\}$$
$$\frac{\mathrm{d}G}{\mathrm{d}\{\theta_1\}} = \left\{ \frac{\mathrm{d}G}{\mathrm{d}\{x^1\}}^T \cdot \frac{\mathrm{d}\{x^1\}}{\mathrm{d}\{\theta_1^1\}} \quad \frac{\mathrm{d}G}{\mathrm{d}\{x^2\}}^T \cdot \frac{\mathrm{d}\{x^2\}}{\mathrm{d}\{\theta_1^2\}} \quad \cdots \quad \frac{\mathrm{d}G}{\mathrm{d}\{x^{I_f}\}}^T \cdot \frac{\mathrm{d}\{x^{I_f}\}}{\mathrm{d}\{\theta_1^{I_f}\}} \right\} \tag{32}$$

where $\mathrm{d}\{x^i\}/\mathrm{d}\{\theta_1^i\}$ can be computed from Eqs. (29–31). The chain rule is then used again to temporally compress the variables:

$$\frac{\mathrm{d}G}{\mathrm{d}\{\theta_{1,\mathrm{dv}}\}} = \frac{\mathrm{d}G}{\mathrm{d}\{\theta_1\}}^T \cdot \frac{\mathrm{d}\{\theta_1\}}{\mathrm{d}\{\theta_{1,\mathrm{dv}}\}} \tag{33}$$

where θ_{dv} are the final design variables associated with the mode: amplitude/phase of a sinusoid, or control points of a cubic spline. The derivative $\mathrm{d}\{\theta_1\}/\mathrm{d}\{\theta_{1,\mathrm{dv}}\}$ is easily computed in the case of sinusoidal motion, though finite differences must be used for the cubic spline, as MATLAB's spline toolbox [38] is used. Furthermore, cost savings are available if the chain-rule transformation $\mathrm{d}\{x^i\}/\mathrm{d}\{\theta_1^i\}$ of Eq. (32) is applied when computing the derivative of the influence matrices [Eq. (19), for example] before the storage of each term and the use of the direct method in Eq. (21).

IV. Flapping-Wing Twist Sensitivities

For the remainder of this work, the wing geometry is fixed as a rectangular planform with an aspect ratio of 6 and a NACA 83XX airfoil (as studied by Fritz and Long [14], where the airfoil thickness parameters are irrelevant for the vortex-lattice method). Six panels are used along the chord and 10 are used along the semispan (root to tip). The flapping amplitude is 45°, and the wing root is given a constant angle of attack (pitch) of 5°. Two reduced frequencies $(k = \omega \cdot c/2/U_\infty)$ of 0.1 and 0.75 are considered; the former is essentially a quasi-steady flight condition, whereas the latter emphasizes unsteady effects. Each flapping period T is discretized into 40 time steps, and a quarter-cycle (10 steps) is needed for the aerodynamic forces to reach time periodicity (i.e., I_o is 10 and I_f is 50).

In this section, only the first twisting mode is considered in demonstrating the performance of the unsteady vortex-lattice method and the subsequent sensitivity analysis. The generalized coordinates of θ_1 form a sinusoidal motion, out of phase with the flapping motion β, following [13], as seen in Fig. 7. Figure 8 provides wake patterns and lift/thrust histories during a flapping cycle when $k = 0.1$. Without the wing twist, the majority of the useful aerodynamic forces (positive lift and thrust) are produced during the downstroke. Though some negative thrust (drag) is produced during the upstroke, the lift is still positive; because the flow is quasi-steady, the angle of attack due to vertical motion [8] (wing flapping) is much smaller than the fixed 5° pitch at the root, and thus the lift remains positive through most of the cycle. As noted by Vest and Katz [13], the thrust during the downstroke is certainly overpredicted, due to an inability to capture viscous flow separation. Without twist, the time-averaged (over the cycle) lift and thrust coefficients are 0.695 and 0.033.

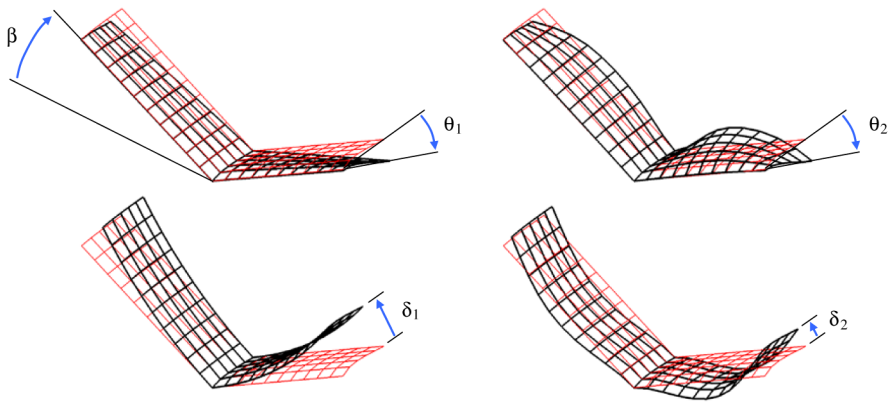

Fig. 6 Morphing wing mode shapes: first twisting (upper left), second twisting (upper right), first bending (lower left), and second bending (lower right).

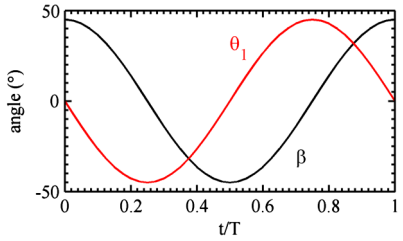

Fig. 7 Flapping and twisting motions used as a baseline study.

Adding twist to the flapping motion (Fig. 8) drastically alters the phase of the lift, with the majority of positive lift now seen in the upstroke. The wing is twisted up during this stroke, providing a large positive angle of attack. These forces also provide a large drag penalty during the upstroke, whereas the thrust during the downstroke is decreased as well. Time-averaged lift and thrust coefficients have dropped to 0.632 and −0.0952. Clearly, for this low reduced frequency, the out-of-phase sinusoidal wing twisting provides additional lift during the upstroke, but hinders all other forces generated during various portions of the flapping stroke. This phase shift in the aerodynamic forces can also be seen in the wake patterns: without twist, the highest circulation within the wake occurs during the downstroke (and thus the peak lift and thrust [17]), and the load is alleviated during the upstroke. With twist, the highest circulation occurs during the upstroke, though the peak values are less.

Results are given in Fig. 9 for a higher reduced frequency of 0.75. For this case, the unsteady terms in Eqs. (7) and (8) ($d\Gamma/dt$) play a significant role in the lift and thrust computations. Furthermore, as the majority of the wake lies very close to the wing, local fluctuations in the wake terms governing the no-penetration equation (4) will become more important. For the untwisted case, as above, the majority of the positive lift is generated during the downstroke, though now the upstroke sees a significant lift penalty. This is due to the fact that at higher flapping frequencies the angle of attack due to wing flapping is much larger than the fixed pitch at the root and is obviously negative during the upstroke. Almost all of the thrust produced during the flapping cycle of the untwisted wing is positive, during both the upstroke and the downstroke. Positive thrust during the downstroke is a result of the negative lift, which is tilted forward as a result of the negative angle of attack to provide the propulsive force [2].

For the untwisted wing, time-averaged lift and thrust coefficients are 1.389 and 1.840, respectively. Including wing twist at $k = 0.75$

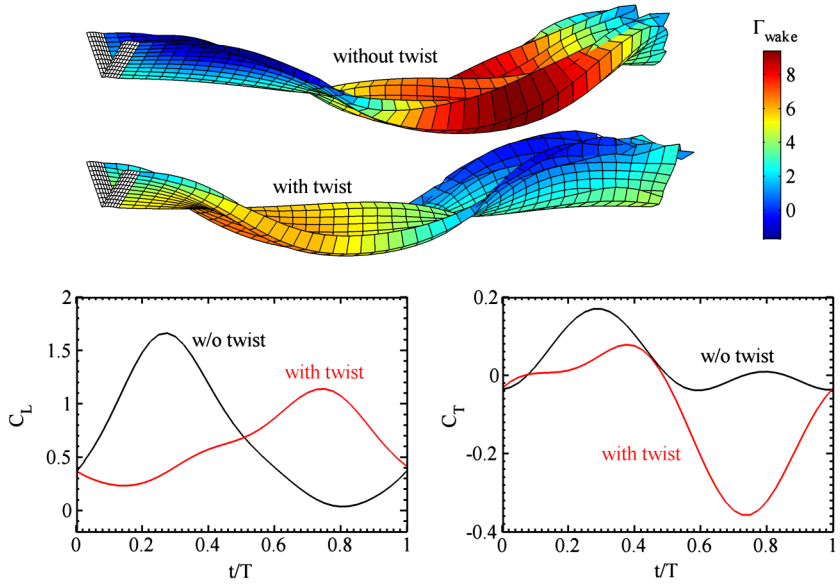

Fig. 8 Wake patterns, lift, and thrust computed during a single flapping cycle at $k = 0.1$, with and without wing twisting.

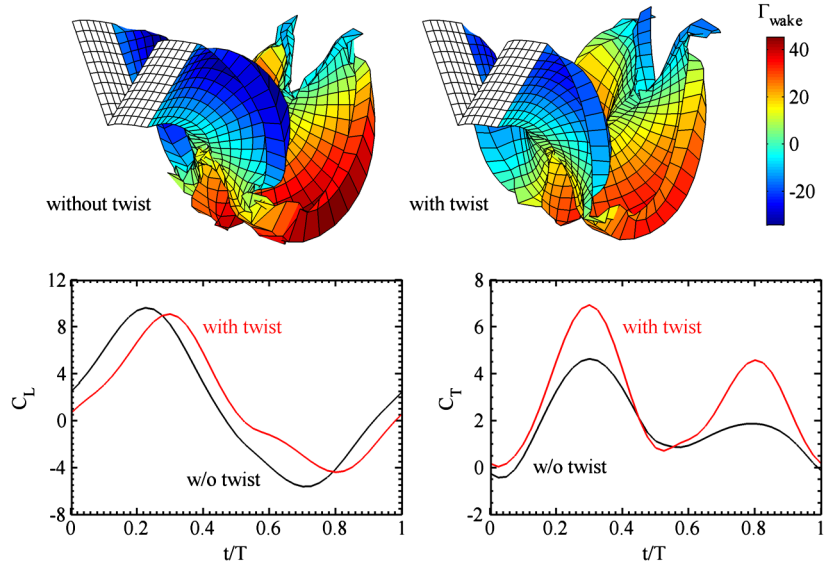

Fig. 9 Wake patterns, lift, and thrust computed during a single flapping cycle at $k = 0.75$, with and without wing twisting.

slightly decreases the magnitude of the maximum and minimum lift values seen during the stroke and introduces a mild phase shift. The effect of wing twist on thrust, however, is very drastic. The feathering motion of the trailing edge decreases the effective angle of attack of each wing section to decrease the drag. The aforementioned lift vector rotation is still present, and the end result is a significant increase in total thrust, during both the up- and downstroke. Similar effects are seen in the wake comparison of Fig. 9, in which the circulation found in the wake of the twisted wing generally has a lower magnitude. This decrease also has ramifications for the input power required for flapping, as will be discussed below. For the twisted wing, the time-averaged lift and thrust coefficients are 1.458 and 2.891; both values are increased over the untwisted case. The effect of wing twist as reported in Figs. 8 and 9 is consistent with the results of Vest and Katz [13]: twisting becomes detrimental toward propulsion as the reduced frequency decreases.

A sensitivity analysis for low-frequency flapping ($k = 0.1$) is given in Fig. 10, in which the objective functions G are considered the time-averaged lift [Eq. (7)], thrust [Eq. (8)], power [Eq. (9)], and propulsive efficiency [Eq. (10)] through the cycle. The design variables are the first-mode twist angle at each time step (θ_1^i), as described in Eq. (32). Flapping with and without wing twist are both considered, and it should be noted that even though the design variable may be zero at each time step (for the untwisted case), $\mathrm{d}G/\mathrm{d}\{\theta_1^i\}$ is typically nonzero. A comparison between the analytical sensitivity analysis given above and a simple (though very expensive) finite difference scheme is also given in the figure, with an excellent agreement between the two.

In terms of the lift coefficients, both the twisted and untwisted cases advocate increasing the twist angle during both the upstroke and the downstroke to increase the time-averaged lift (as evidenced from the positive values of $\mathrm{d}G/\mathrm{d}\theta^i$). For this quasi-steady flight condition, increasing the twist angle will increase the angle of attack and thus the lift. The untwisted wing is closer to an optimum during the upstroke (as the gradients are smaller), whereas the twisted wing is superior during the downstroke. This is further confirmed with the lift trends seen in Fig. 8. The extremely detrimental effect of wing twist upon thrust (for low reduced frequencies) is seen in the derivatives of the time-averaged thrust of the twisted wing of Fig. 10. During the downstroke, when the twist is negative, the derivatives are strongly positive, suggesting that increasing the twist will improve thrust. The opposite is seen during the upstroke. Contrastingly, the derivatives of the untwisted wing are very small, though a small amount of negative twist is recommended during the upstroke. As before, these trends are generally verified by an inspection of Fig. 8.

For the untwisted wing in Fig. 10, the input power can be decreased with wash-out during the downstroke and wash-in during the upstroke. For the twisted wing, however [which uses this exact twist profile (Fig. 7)], the derivatives have changed signs, suggesting that the optimum lies at a twisting amplitude less than 45°. The propulsive efficiency η [Eq. (10)] is increased by decreasing the twist during both the up- and downstroke, presumably to lower the angle of attack. As mentioned above, increasing (or at least maintaining) the coefficient of lift of the untwisted wing requires an increase in the twist angle during both strokes: efficiency and lift cannot simultaneously be improved using the first twisting mode when $k = 0.1$, as will be discussed below.

Sensitivity derivatives for the larger reduced frequency (0.75) are given in Fig. 11. As above, time-averaged lift, thrust, power, and efficiency derivatives; twisted and untwisted wings; and analytical and finite difference computations are all given, with an excellent comparison between the latter two. The derivatives for the low-reduced-frequency case are relatively smooth, though this is no longer the case at higher frequencies. The response is particularly noisy at the end of each stroke ($t/T = 0, 0.5, 1$), where the unsteady term $\mathrm{d}\Gamma/\mathrm{d}t$ is largest. As the wing passes through the midplane, the derivatives are fairly smooth. The sensitivities in Fig. 10 also show noisy behavior at $t/T = 0$ and 1, but not at 0.5; these are probably due to unequal weighting ω^i of the end points in the integration scheme and also contribute to the data in Fig. 10. The noisy derivatives are further indication that a temporal link must be provided using a sinusoidal or spline-based approximation [Eq. (33)] for the optimizer, or the optimal design will have unrealistic accelerations from one time step to the next.

The untwisted wing sensitivities advocate negative twist during the downstroke for greater lift, whereas the twisted wing (which has negative twist during the downstroke) recommends the opposite: obviously, an optimum lies somewhere in between. Overall, lift derivatives are fairly small, however, indicative of the minor changes in C_L due to wing twist seen in Fig. 9. Similar contrasts are seen with the thrust, where the untwisted wing indicates negative twist during the downstroke and the opposite during the upstroke to maximize

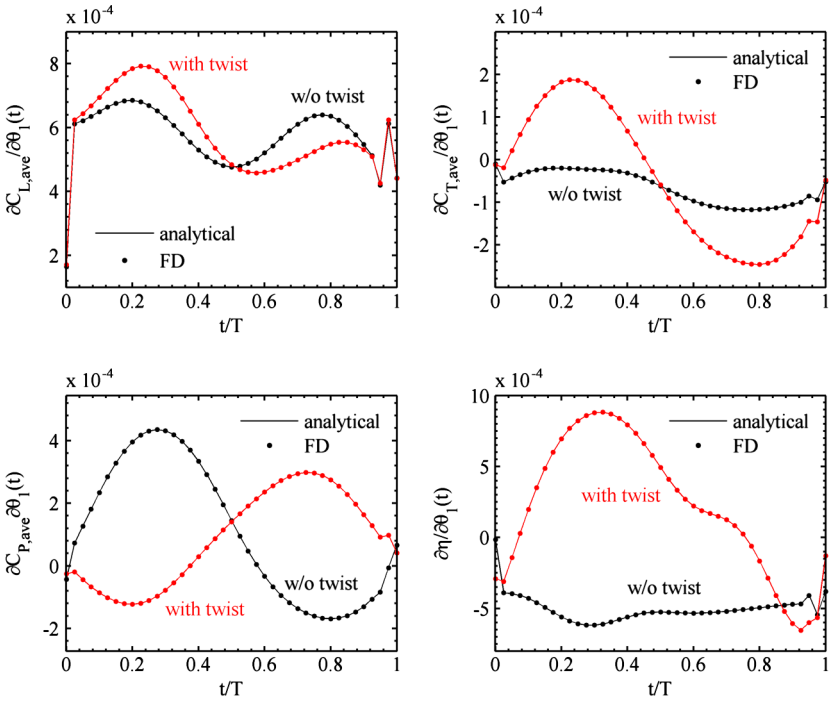

Fig. 10 Derivatives of time-averaged lift (upper left), thrust (upper right), power (lower left), and efficiency (lower right) with respect to the wing twist (first mode) at each time step, $k = 0.1$.

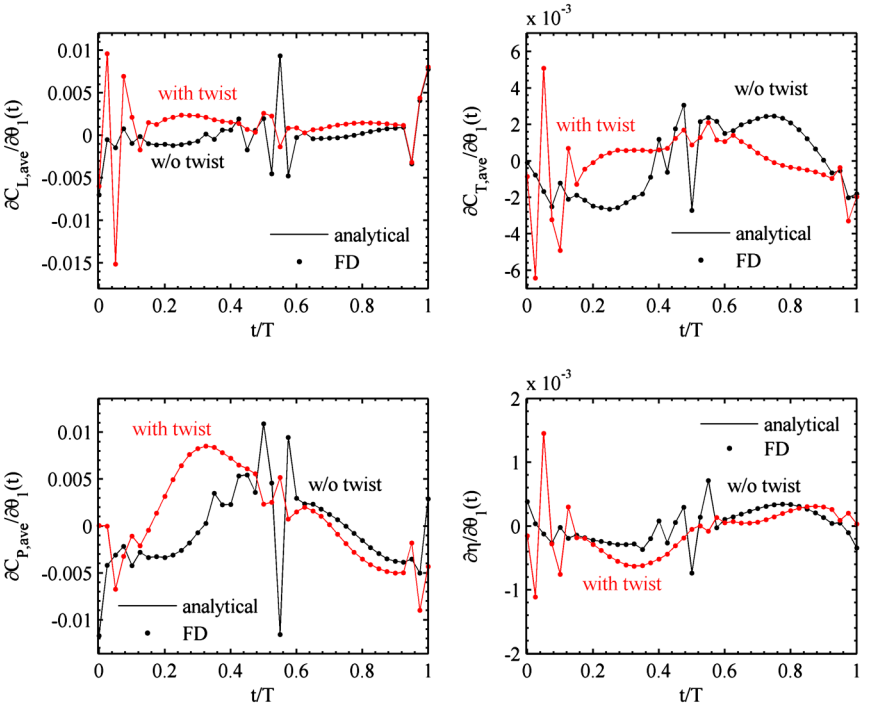

Fig. 11 Derivatives of time-averaged lift (upper left), thrust (upper right), power (lower left), and efficiency (lower right) with respect to the wing twist (first mode) at each time step, $k = 0.75$.

thrust. The twisted wing, which uses that exact design strategy, indicates that the twist may be too low toward the end of the downstroke and too high at the end of the upstroke, where the flapping velocity approaches zero and high forces typically translate into a drag.

As may be expected, the design space for power (and subsequently the efficiency) is fairly complex for higher reduced frequencies. For the power terms in Fig. 11 the untwisted wing is able to decrease the input power by increasing the twist during both the up- and downstroke, though wash-out is preferred at the bottom of the downstroke. Conversely, the twisted wing (with negative twist during the downstroke) can decrease the power by further decreasing the twist for this portion of the flapping cycle: this trend suggests multiple local optima. During the upstroke, both the twisted and untwisted wings have very similar sensitivities, despite drastically different twist profiles. For the efficiency terms, an out-of-phase twist profile similar to that of Fig. 7 will improve η. As the efficiency derivatives are not in direct opposition to either the lift or thrust derivatives for the entire cycle (such as seen with the lift in Fig. 10), it should be possible to improve the propulsive efficiency without degrading the force-producing capabilities of the wing.

Having studied the derivatives of the cycle-averaged force terms, attention is now briefly turned to the sensitivities of forces at a given time step ($\partial g^i/\partial\{x^j\}$), as computed with Eq. (20). Results are given for an untwisted wing in Fig. 12 for both low and high reduced frequencies. The derivative of the lift coefficient at the middle and the end of the cycle ($t/T = 0.5$ and 1) is given with respect to the first-mode twist angle at each preceding time step. When the reduced frequency is 0.1, $\partial g^i/\partial\{x^j\}$ is largest when i and j coincide and rapidly and smoothly drops off as one moves backward in time. Only the wake terms can provide the force computations at one step with the influence of the geometry at a preceding step; for the low reduced frequencies, the wake is too far from the wing to have a sizeable impact.

In light of this result, only the geometry information at the preceding few time steps is needed for an accurate computation of Eq. (14): the reverse summation can be truncated with little loss of accuracy. For the higher reduced frequency, however, this is not necessarily the case. As expected, the gradients are very noisy in time, and certain portions of the history have relevant magnitudes toward the complete computation of Eq. (14) (particularly when j lags i by a half-cycle). Furthermore, $\partial g^i/\partial\{x^j\}$ is largest when $j = i - 1$; this is thought to be due to the fact that many unsteady terms are computed with a backward finite difference, which obviously become more relevant at higher reduced frequencies.

V. Design Optimization Applications

The final section of this work uses the above techniques to optimize the propulsive efficiency of a flapping wing with active shape morphing, subject to force-based constraints, as discussed by Berman and Wang [4]:

$$\begin{aligned} &\text{maximize } \eta \\ &\text{such that } C_{L,\text{ave}} \geq C_{L,\text{baseline}} \\ &\qquad C_{T,\text{ave}} \geq C_{T,\text{baseline}} \\ &\qquad \text{KS}^i \leq 0 \qquad i = I_o, \ldots, I_f \\ &\qquad \{\text{LB}\} \leq \{\theta_{\text{DV}}\} \leq \{\text{UB}\} \end{aligned}$$

where $C_{L,\text{baseline}}$ and $C_{T,\text{baseline}}$ are the cycle-averaged coefficients computed without shape morphing:, i.e., the results of Figs. 8 and 9 for the untwisted wing. These first two constraints should not

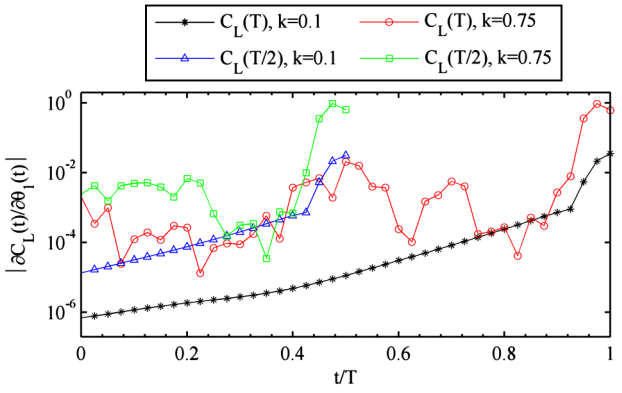

Fig. 12 Derivative of the lift coefficient at $t/T = 0.5$ and 1 with respect to the wing twist at all preceding time steps, for an untwisted wing.

necessarily be thought of as trim requirements (which should be considered at each time step, rather than the cycle-averaged quantities used here), but merely as ensuring that the optimization process does not remove the basic force-producing ability of the baseline wing during its search for efficiency improvements. As the current work is solely concerned with wing design, longitudinal stability (i.e., pitching moment) is not considered. KS is a Kreisselmeier–Steinhauser function [21] computed over the wing at each time step:

$$\mathrm{KS}^{\,i} = \frac{1}{\kappa} \cdot \ell_n \left(\sum_{m=1}^{M+1} \sum_{n=1}^{N+1} \left(e^{\kappa \cdot (z^i_{m,n} - z_{o,m,n} - w_{\max})} \right) \right) \tag{34}$$

This function essentially requires that the out-of-plane morphing deformation at each node ($\{z^i\} - \{z_o\}$) is less than a given value $w_{\max}$. The nonlinear exponential terms places the greatest weight upon the constraint with the largest violation (the node with the largest deformation above $w_{\max}$). The morphing deformation can be computed with Eq. (31), as can the sensitivities of the KS function with respect to the wing geometry ($\partial \mathrm{KS}^i / \partial \{x^i\}$). A separate KS function is computed at each time step within the cycle, with κ set to 150 and $w_{\max}$ set to 70% of the root chord.

The final constraint establishes side constraints for the vector of design variables. The generalized coordinates of each wing mode (Fig. 6) are constrained by bounding either the amplitudes (for an assumed sinusoidal motion) or the values at the control points of the cubic spline approximation. As noted in Table 1, the first twisting mode θ_1 is bounded by $\pm 45°$, the second twisting mode is bounded by $\pm 20°$, the first bending mode δ_1 is bounded by $\pm 0.7 \cdot c$, and the second bending mode δ_2 is bounded by $\pm 0.3 \cdot c$. For the spline motions, this will only control the deformation at time steps that coincide with a control point location; intermediate time steps will be limited by the KS function of Eq. (34). No penalty is applied during the optimization process associated with morphing actuation: i.e., feasible actuator placement along the wing to actually achieve shapes described below. While such a constraint should certainly be applied during the flapping-wing design process [as well as the power required to morph the wings, which is not included in Eq. (9)], the current study is merely intended to demonstrate the usefulness of an analytical sensitivity analysis for vortex-lattice-method-based optimization and to provide a set of primary design guidelines for efficient flapping flyers via wing deformation.

Table 1 Summary of generalized coordinate bounds

Wing morphing	Lower bound	Upper bound
θ_1: first twisting mode	$-45°$	$45°$
θ_2: second twisting mode	$-20°$	$20°$
δ_1: first bending mode	$-0.7 \cdot c$	$0.7 \cdot c$
δ_2: second bending mode	$-0.3 \cdot c$	$0.3 \cdot c$

All optimization studies are run with MATLAB's `fmincon` function [38], which uses sequential quadratic programming with a quasi-Newton approximation to the Hessian. Sensitivities of the objective function and constraints are supplied to the algorithm using the above framework. As discussed above, several optimization runs are conducted with an increasing number of design variables (providing a greater degree of spatial and temporal freedom to the active shape morphing). The optimal design from one run can be used as an initial guess for the next run with a larger number of design variables. Results from the sweep of optimization runs are given in Tables 2 and 3 for reduced frequencies of 0.1 and 0.75, respectively.

For all cases, the constraint upon the cycle-averaged lift coefficient remains active, and the propulsive efficiency generally increases as the number of design variables N_{DV} increases. Efficiency values are generally larger as the reduced frequency is increased, consistent with data given by Vest and Katz [13]. At low reduced frequencies (Table 2), sinusoidal first-mode bending or twisting (two design variables) is unable to improve the propulsive efficiency without violating one or more of the constraints, though a combination of the two (four design variables) provides mild improvements. For high reduced frequencies (Table 3), sinusoidal first-mode twisting is very successful by pushing the amplitude to 45°; efficiency is optimal with a phase shift of 1.33, though thrust is optimal with a phase of 1.57, as seen in Fig. 7. Sinusoidal first-mode bending is, as before, unable to improve efficiency in a feasible manner, and optimizing with first-mode bending and twisting (four design variables) reverts to the solution with only twisting.

As would be expected, providing a greater degree of temporal freedom (i.e., cubic splines, rather than a sinusoidal approximation) greatly improves the optimal design for both reduced frequencies. It should also be noted that no discernible difference in computational cost was noted in gradient computations for any of the cases in Table 2 or Table 3. As discussed above, Eq. (21) requires the solution to a system of equations with multiple right-hand sides (one for each design variable), which is very fast for the moderately sized matrices considered here. This is in stark contrast to the use of finite differences (such as seen in Figs. 10 and 11), for which the computational cost is proportional to the number of design variables.

Considering only first-mode bending and twisting (14 design variables), phase plots of the optimal generalized coordinates θ_1 and δ_1 are given for both reduced frequencies in Fig. 13. The wing shapes that results from these motions are given in Fig. 14; care should be taken in interpreting the latter plots, as the apparent forward speed of

Table 2 Optimal design results, $k = 0.1$

Wing morphing	N_{DV}	$C_{L,\mathrm{ave}}$	$C_{T,\mathrm{ave}}$	$C_{P,\mathrm{ave}}$	η	Optimal solution
None, baseline	0	0.695	0.033	0.171	0.191	——
First twisting mode, sinusoidal	2	0.695	0.033	0.171	0.191	$\theta_1 = 0$
First bending mode, sinusoidal	2	0.695	0.033	0.171	0.191	$\delta_1 = 0$
First bending and twisting modes, sinusoidal	4	0.695	0.035	0.165	0.213	$\theta_1 = 8.94° \cdot \sin(\omega \cdot t - 0.008)$ $\delta_1 = (0.693 \cdot c) \cdot \sin(\omega \cdot t - 1.55)$
First bending and twisting modes, spline	14	0.695	0.046	0.166	0.281	Fig. 13
First and second bending and twisting modes, spline	28	0.695	0.072	0.163	0.440	Fig. 15

Table 3 Optimal design results, $k = 0.75$

Wing morphing	N_{DV}	$C_{L,\mathrm{ave}}$	$C_{T,\mathrm{ave}}$	$C_{P,\mathrm{ave}}$	η	Optimal solution
None, baseline	0	1.389	1.840	7.371	0.249	——
First twisting mode, sinusoidal	2	1.389	2.557	4.898	0.522	$\theta_1 = 45° \cdot \sin(\omega \cdot t + 1.33)$
First bending mode, sinusoidal	2	1.389	1.840	7.371	0.249	$\delta_1 = 0$
First bending and twisting modes, sinusoidal	4	1.389	2.557	4.898	0.522	$\theta_1 = 45° \cdot \sin(\omega \cdot t + 1.33)$ $\delta_1 = 0$
First bending and twisting modes, spline	14	1.389	2.142	3.413	0.627	Fig. 13
First and second bending and twisting modes, spline	28	1.389	2.021	2.589	0.781	Fig. 16

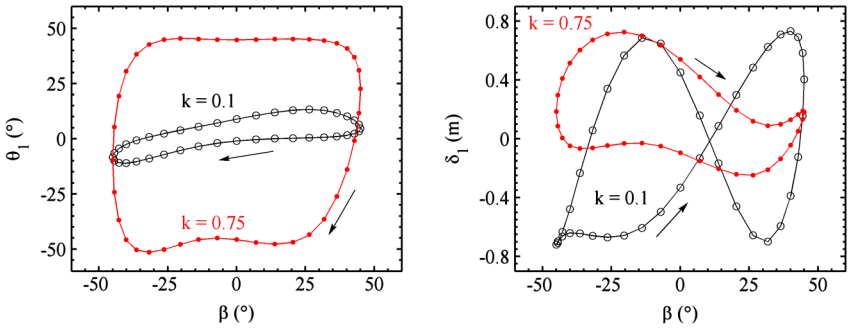

Fig. 13 Optimal wing morphing with first-mode twisting and bending: generalized coordinates approximated with cubic splines, plotted versus flapping angle β.

the wing is scaled so as to see each wing shape clearly and is not indicative of the true reduced frequency. Certain portions of the phase plots may appear to violate the deformation constraints, but all designs are feasible. Toward the end of the downstroke ($k = 0.75$), for example, the first-mode twisting amplitude becomes $-52°$. As seen in Fig. 6, this entails a large upward deflection of the trailing edge, which is partially counteracted by the negative bending in this portion of the stroke, and the end result is feasible with respect to the KS constraint of Eq. (34). Regardless, the values of the amplitudes at the spline control points ($t/T = 0, 1/7, \ldots, 6/7$) all lie within the restrictive side constraints ($\pm 45°$ for first-mode twisting).

For the lower reduced frequency ($k = 0.1$), a moderate amount of first-mode wing twist is used in conjunction with a large amount of first-mode wing bending, the latter operating at roughly twice the flapping frequency. Wing velocities due to the first-mode bending are relatively large through the midstroke (increasing flapping velocities during the upstroke, though counteracting the motion during the downstroke) as well as at the top of the upstroke. The reduced frequency is too low in this case for the velocity of the first-mode bending to make a substantial contribution to the angle of attack of each section, however, and so the drastic changes in shape are the probable cause of the efficiency improvements. Through the first portion of the downstroke, the bending motion acts to counteract the flapping motion entirely: as seen in Fig. 14, the untwisted wingtip motion is very minor. Presumably, this is a power-optimal solution. Similarly, the wingtip motion is counteracted at the bottom of the downstroke, remaining negatively twisted with a strong anhedral for a significant portion of the stroke.

For the higher reduced frequency ($k = 0.75$), the wing twist has a large magnitude and is mostly out of phase with the flapping motion, as above; the optimal feathering motion bears similarities with results given by Willis et al. [17]. Through the upstroke, the wing twist is largely constant at 45°, though larger magnitudes are seen during the downstroke, as discussed above. First-mode wing bending is much more moderate for this case (both magnitudes and velocities) and appears to be used to control the axis about which the wing rotates (as well as to allow large rotations without violating the KS constraint). Through the downstroke, wing bending is minor, and so the wing rotates about the leading edge, as specified by the mode shape in Fig. 6. Conversely, through the upstroke, the positive wing bending shifts the center of rotation toward the midchord, as seen in Fig. 14.

Turning now to optimal wing motions with all four mode shapes considered (28 design variables), phase plots of the four generalized coordinates are given in Fig. 15 ($k = 0.1$) and Fig. 16 ($k = 0.75$), and the resulting wing motions are given in Fig. 17. For the low reduced frequency, a very moderate amount of second-mode twisting is used, which allows a larger first-mode amplitude than previously seen at this frequency. The first bending mode still operates at roughly twice the flapping frequency, though is now skewed toward the top of the upstroke. The amplitude of this mode seen in Fig. 15 is very large as

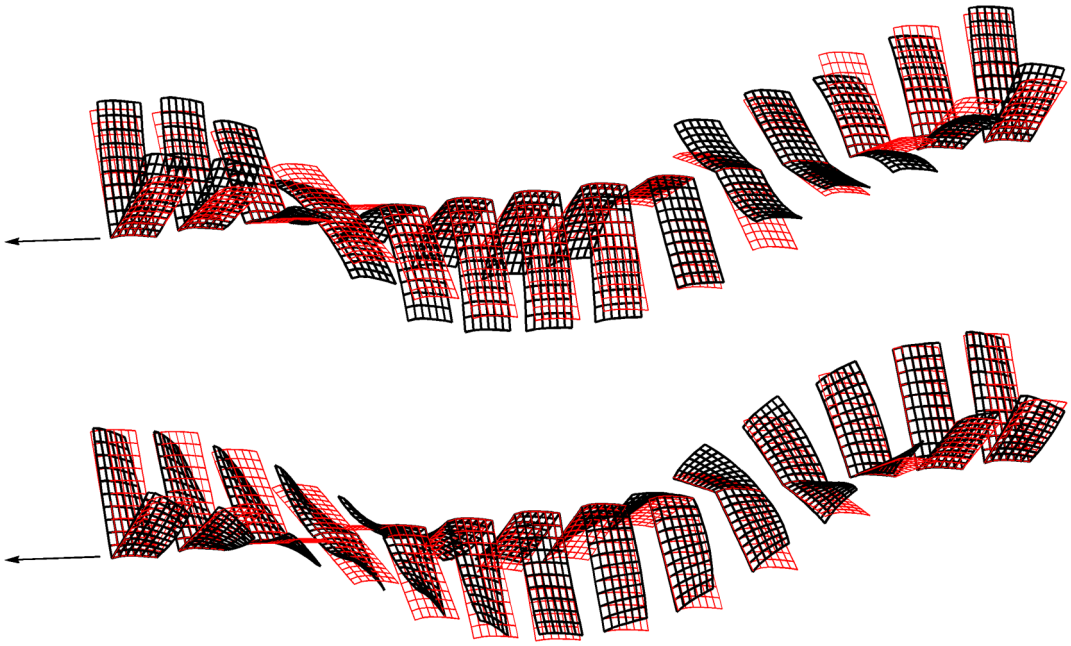

Fig. 14 Baseline (thin lines) and morphed shapes (thick lines) described by Fig. 13 through the stroke: $k = 0.1$ (top) and $k = 0.75$ (bottom). Apparent distance traveled by wing is scaled.

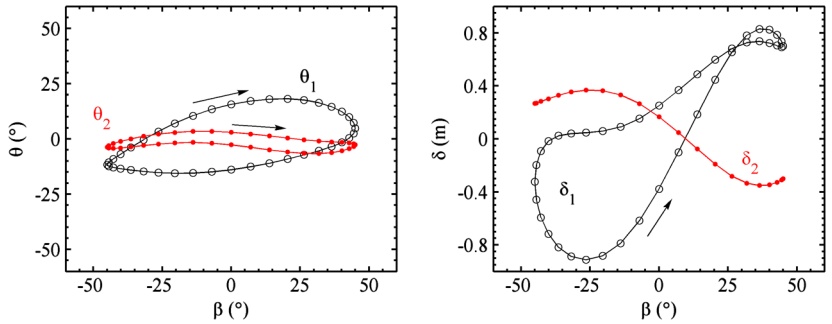

Fig. 15 Optimal wing morphing with first- and second-mode twisting and bending for $k = 0.1$: generalized coordinates approximated with cubic splines, plotted versus flapping angle β.

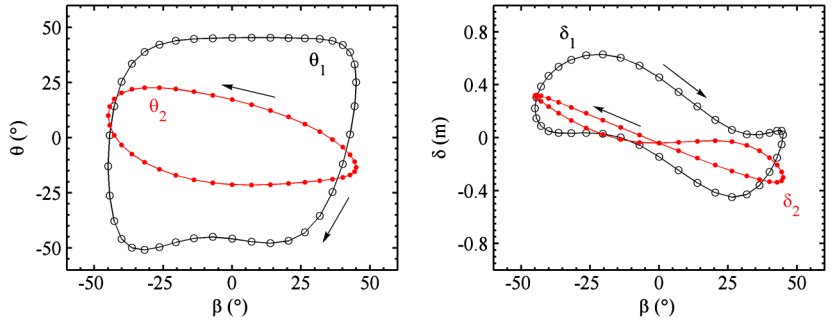

Fig. 16 Optimal wing morphing with first- and second-mode twisting and bending for $k = 0.75$: generalized coordinates approximated with cubic splines, plotted versus flapping angle β.

well, though deflection values at the wingtip are offset by the second-mode bending, which is typically of opposite sign. This combined motion forces large deformations toward the inboard portion of the flapping wing, clearly seen in Fig. 17. The second-mode bending amplitude has no phase loop, as the motion along the upstroke is identical to that along the downstroke.

Similar trends can be seen at the higher reduced frequency (Fig. 16), though the twisting deformations are more relevant for this case. The first-mode and second-mode twisting travel in separate directions along the phase loop, so that they typically have opposite signs. As before, this causes large deformations toward the inboard portions of the wing, forcing a larger portion of the wing to twist. Bending again appears to be used to control the chordwise location about which the wing rotates (where the midchord is preferred during the upstroke). Furthermore, the ratio of first-mode and second-mode bending is tailored at each time step so that the amplitude of the path traveled by the wingtip is much less than for the undeformed wing during the complete flapping cycle.

The lift, thrust, and power phase plots that develop over the flapping wing at $k = 0.1$ are given in Fig. 18 for both first-mode spline morphing (Fig. 14) and first- and second-mode spline morphing (Fig. 17). Morphing with only the first modes generally

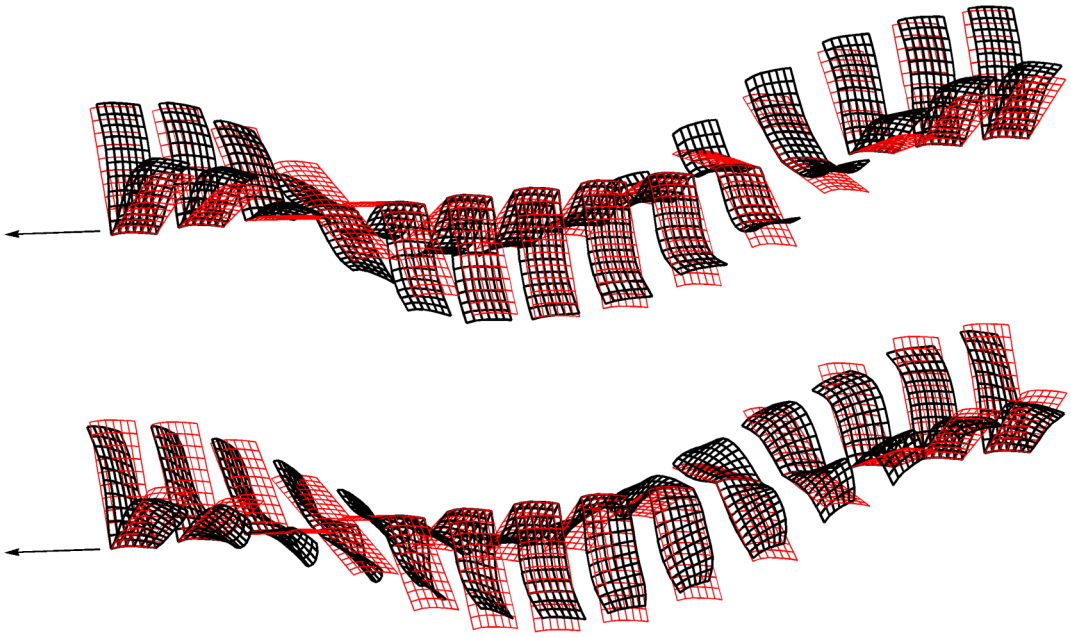

Fig. 17 Baseline (thin lines) and morphed shapes (thick lines) described by Figs. 15 and 16 through the stroke: $k = 0.1$ (top) and $k = 0.75$ (bottom). Apparent distance traveled by the wing is scaled.

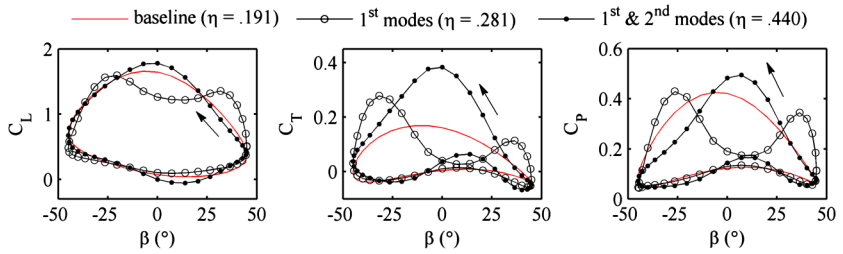

Fig. 18 Lift, thrust, and power computed as a function of flapping angle for the spline morphing optimization, $k = 0.1$.

decreases the forces (lift, thrust, and power) through the middle of the downstroke (as discussed above, the local bending deformation counteracts the flapping motion, and the wing position remains nearly constant, as seen in Fig. 14). Forces are redistributed to the beginning and end of the downstroke: the lift constraint is fulfilled, and the ratio of average thrust and power is such that propulsive efficiency improves (from 0.191 to 0.281). For combined first- and second-mode spline morphing, the motions at the middle of the downstroke increase the forces (though power decreases during the latter portion of the stroke), whereas the forces at the extremes of the flapping stroke are largely unchanged. The introduction of the second modes improves the thrust during the upstroke as well (though lift and power suffer): the end result is a further increase in efficiency to 0.440.

Similar results are given in Fig. 19 for a reduced frequency of 0.75. Unlike the previous case, in which the introduction of the second modes gives entirely different optimal force trends, both optimization cases give similar results here, with the second modes providing a more drastic response. For the lower reduced frequency, optimal efficiency is thrust-based, as only minor improvements in power are available, though the opposite is true at higher reduced frequencies (as seen in Tables 2 and 3). Providing the system with greater degrees of freedom for morphing generally collapses the lift phase plot, where the loss of lift generation during the downstroke is offset by the negative lift typically generated through the upstroke, leaving the lift constraint active. As mentioned, minor changes in thrust are seen over the cycle, but the required input power drops dramatically over both the upstroke and the downstroke, leaving efficiencies of 0.627 and 0.781 for first- and second-mode morphing, respectively.

The sectional normal force coefficient computed along the semispan of the flapping wing is given in Fig. 20 for a reduced frequency of 0.1. Results are given for the three cases discussed in Fig. 18, from left to right: the top of the upstroke, the middle of the downstroke, the bottom of the downstroke, and the middle of the upstroke. As noted above, the predominate differences between the baseline and the two morphing schemes are clearly seen through the downstroke: morphing with only the first modes decreases the forces (as compared with the baseline case) and vice versa for first- and second-mode morphing. The forces for the latter case are peak at 60% of the semispan, as the use of the second bending and twisting

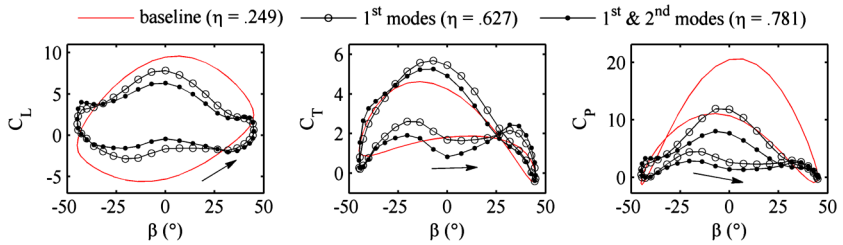

Fig. 19 Lift, thrust, and power computed as a function of flapping angle for the spline morphing optimization, $k = 0.75$.

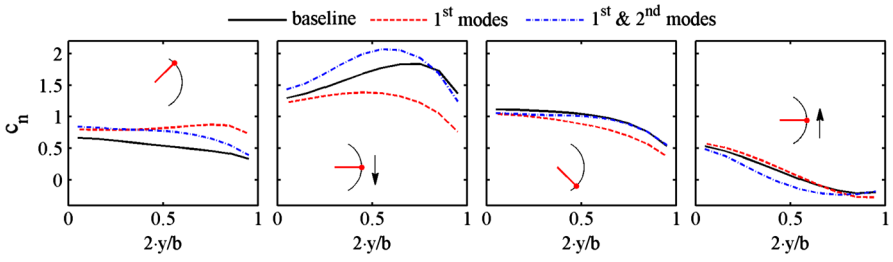

Fig. 20 Sectional normal force coefficient along the semispan for the spline morphing optimization, $k = 0.1$.

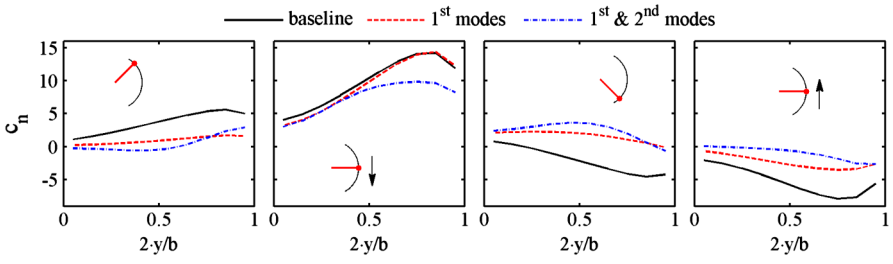

Fig. 21 Sectional normal force coefficient along the semispan for the spline morphing optimization, $k = 0.75$.

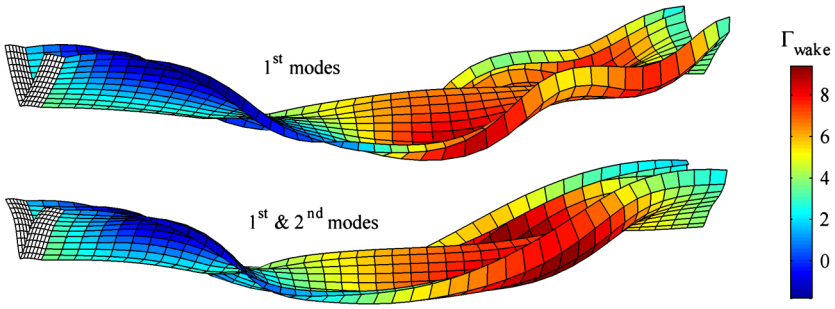

Fig. 22 Wake patterns aft of the flapping wing with optimal morphing, $k = 0.1$.

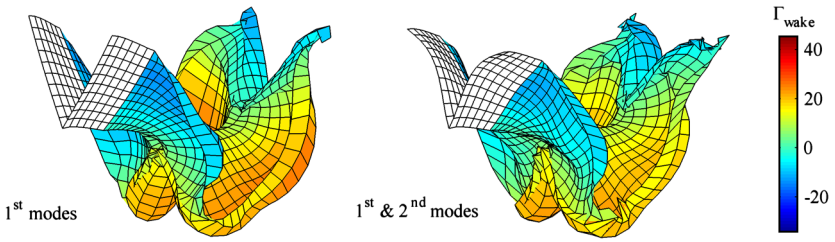

Fig. 23 Wake patterns aft of the flapping wing with optimal morphing, $k = 0.75$.

modes provides large inboard deformations (Fig. 17). Further results are given in Fig. 21 for a reduced frequency of 0.75. Both optimal designs are generally capable of decreasing the forces as compared with the baseline case (and thus, presumably, the input power seen in Fig. 19) along the wing during the entire flapping motion, though morphing with both first and second modes is substantially more effective through the middle of the downstroke.

Finally, the circulation strength of the wakes trailing the optimal wing morphing configurations discussed above are given in Figs. 22 and 23 for low and high reduced frequencies. Both first-mode morphing and first- and second-mode morphing are given. The axis limits of the contour plots are identical to their counterparts in Fig. 8 and Fig. 9 for comparison with baseline (undeformed) wing flapping. When $k = 0.1$ (Fig. 22), the overall strength of the wake has not substantially decreased from the baseline case, as the average power decrease is minor. The local drop in power through the middle of the downstroke with first-mode morphing (Fig. 18) is evident from the wake panels, which are aligned with the forward-flight direction during this portion of the stroke. When $k = 0.75$ (Fig. 23), the vortex rings in the wake are substantially weaker than the baseline case, reflective of the large drop in required input power.

VI. Conclusions

This work has detailed a computational framework capable of obtaining the derivative of a time-averaged force quantity (lift, thrust, power, propulsive efficiency) with respect to the shape of a flapping wing at any time step. These sensitivities are computed analytically with an unsteady vortex-lattice method, by differentiating the no-penetration condition for each panel that is used to build the system of equations. For low reduced frequencies, the flow that develops over the flapping wing is essentially quasi-steady: the aerodynamic state at a given time step is mostly influenced by the wing shape at that time step. As the reduced frequency increases, unsteady effects become important, the influence of the wake is stronger, and the forces at a time step are substantially affected by the wing shape at previous time steps. Wake terms provide the only connection between the forces generated at disparate time steps and must be included to compute accurate sensitivities.

These derivatives are used for gradient-based optimization to maximize the propulsive efficiency under lift and thrust constraints. As expected, increasing the number of design variables (providing the wing morphing with a greater degree of spatial and temporal freedom) provides higher efficiencies. At low reduced frequencies, bending deformation plays a large role, substantially increasing the time-averaged thrust to improve the efficiency, though the average power is largely unaffected. At high reduced frequencies, twisting deformations are more important; optimization drives the design to a morphing configuration with very low input power, though the time-averaged thrust only shows minor improvements.

This work has many relevant future applications. First, and most obvious, the morphing designs obtained above can be tested with higher-fidelity aerodynamic solvers to ascertain their superiority over the baseline configuration. Results from these tests may provide some indication of additional constraints needed to avoid configurations known to exhibit massive viscous flow separation, for example. Second, the results above may provide a suitable framework for jig-shape aerostructural optimization. As the optimal cyclic wing shape as well as the concomitant pressure distribution are known, these aerodynamic forces can be applied to a structural model to compute passive deformation. The internal layout of the wing structure can be optimized until the resulting deformed wing shape matches the results given above. This decoupled aeroelastic optimization will surely give suboptimal results (and in some cases may be unable to approach the complex deformations computed above), leading to a third application. A fully coupled aeroelastic sensitivity analysis would require the derivative of the aerodynamic state with respect to the wing shape at each time step, as detailed above. The framework given in this paper should be immediately applicable to such an undertaking.

Acknowledgments

This work is sponsored by the U.S. Air Force Office of Scientific Research under Laboratory Task 09RB01COR monitored by John Schmisseur. This research was performed while the first author held a National Research Council Associateship Award at the U.S. Air Force Research Laboratory.

References

[1] Le Moigne, A., and Qin, N., "Variable-Fidelity Aerodynamic Optimization for Turbulent Flows Using a Discrete Adjoint Formulation," *AIAA Journal*, Vol. 42, No. 7, 2004, pp. 1281–1292. doi:10.2514/1.2109

[2] Shyy, W., Berg, M., and Ljungsqvist, D., "Flapping and Flexible Wings for Biological and Micro Air Vehicles," *Progress in Aerospace Sciences*, Vol. 35, No. 5, 1999, pp. 455–505. doi:10.1016/S0376-0421(98)00016-5

[3] Lee, J., Kim, J., and Kim, C., "Numerical Study on the Unsteady-Force-Generation Mechanism of Insect Flapping Motion," *AIAA Journal*, Vol. 46, No. 7, 2008, pp. 1835–1848. doi:10.2514/1.35646

[4] Berman, G., and Wang, Z., "Energy-Minimizing Kinematics in Hovering Insect Flight," *Journal of Fluid Mechanics*, Vol. 582, 2007, pp. 153–168. doi:10.1017/S0022112007006209

[5] Beran, P., Parker, G., Snyder, R., and Blair, M., "Design Analysis Strategies for Flapping Wing Micro Air Vehicles," *International Forum on Aeroelasticity and Structural Dynamics*, KTH Royal Inst. of Technology, Paper IF-109, Stockholm, June 2007.

[6] Rakotomamonjy, T., Ouladsine, M., and Le Moing, T., "Modelization and Kinematics Optimization for a Flapping-Wing Microair Vehicle," *Journal of Aircraft*, Vol. 44, No. 1, 2007, pp. 217–231. doi:10.2514/1.22960

[7] Madangopal, R., Khan, Z., and Agrawal, S., "Biologically Inspired Design of Small Flapping Wing Air Vehicles Using Four-Bar Mechanisms and Quasi-Steady Aerodynamics," *Journal of Mechanical Design*, Vol. 127, No. 4, 2005, pp. 809–816. doi:10.1115/1.1899690

[8] Shyy, W., Lian, Y., Tang, J., Liu, H., Trizila, P., Stanford, B., Bernal, L., Cesnik, C., Friedman, P., and Ifju, P., "Computational Aerodynamics of Low Reynolds Number Plunging, Pitching and Flexible Wings for MAV Applications," *Acta Mechanica Sinica*, Vol. 24, No. 4, 2008, pp. 351–373. doi:10.1007/s10409-008-0164-z

[9] Ho, S., Nassef, H., Pornsinsirirak, N., Tai, Y., and Ho, C., "Unsteady Aerodynamics and Flow Control for Flapping Wing Flyers," *Progress in Aerospace Sciences*, Vol. 39, No. 8, 2003, pp. 635–681. doi:10.1016/j.paerosci.2003.04.001

[10] Tuncer, I., and Kaya, M., "Optimization of Flapping Airfoils for Maximum Thrust and Propulsive Efficiency," *AIAA Journal*, Vol. 43, No. 11, 2005, pp. 2329–2336. doi:10.2514/1.816

[11] Soueid, H., Guglielmini, L., Airiau, C., and Bottaro, A., "Optimization of the Motion of a Flapping Airfoil Using Sensitivity Functions," *Computers and Fluids*, Vol. 38, 2009, pp. 861–874. doi:10.1016/j.compfluid.2008.09.012

[12] Katz, J., and Plotkin, A., *Low-Speed Aerodynamics*, Cambridge Univ. Press, Cambridge, MA, 2001.

[13] Vest, M., and Katz, J., "Unsteady Aerodynamic Model of Flapping Wings," *AIAA Journal*, Vol. 34, No. 7, 1996, pp. 1435–1440. doi:10.2514/3.13250

[14] Fritz, T., and Long, L., "Object-Oriented Unsteady Vortex Lattice Method for Flapping Flight," *Journal of Aircraft*, Vol. 41, No. 6, 2004, pp. 1275–1290. doi:10.2514/1.7357

[15] Smith, M., "Simulating Moth Wing Aerodynamics: Towards the Development of Flapping-Wing Technology," *AIAA Journal*, Vol. 34, No. 7, 1996, pp. 1348–1355. doi:10.2514/3.13239

[16] Zhu, Q., "Numerical Simulation of a Flapping Foil with Chordwise or Spanwise Flexibility," *AIAA Journal*, Vol. 45, No. 10, 2007, pp. 2448–2457. doi:10.2514/1.28565

[17] Willis, D., Israeli, E., Persson, P., Drela, M., Peraire, J., Swartz, S., and Breuer, K., "A Computational Framework for Fluid Structure Interaction in Biologically Inspired Flapping Flight," AIAA Applied Aerodynamics Conference, Miami, FL, AIAA Paper 2007-3803, June 2007.

[18] Hall, K., Pigott, S., and Hall, S., "Power Requirements for Large-Amplitude Flapping Flight," *Journal of Aircraft*, Vol. 35, No. 3, 1998, pp. 352–361. doi:10.2514/2.2324

[19] Lebental, S., "Optimization of the Aerodynamics of Small-Scale Flapping Aircraft in Hover," Ph.D. Thesis, Dept. of Mechanical Engineering and Science, Duke Univ., Durham, NC, 2008.

[20] van Keulen, F., Haftka, R., and Kim, H., "Review of Options for Structural Design Sensitivity Analysis. Part 1: Linear Systems," *Computer Methods in Applied Mechanics and Engineering*, Vol. 194, No. 30, 2005, pp. 3213–3243. doi:10.1016/j.cma.2005.02.002

[21] Haftka, R., and Gürdal, Z., *Elements of Structural Optimization*, Kluwer Academic, Dordrecht, The Netherlands, 1991.

[22] Kim, N., and Choi, K., "Design Sensitivity Analysis and Optimization of Nonlinear Transient Dynamics," AIAA Symposium on Multidisciplinary Analysis and Optimization, Long Beach, CA, AIAA Paper 2000-4905, Sept. 2000.

[23] Trier, S., Marthinsen, A., and Sivertsen, O., "Design Sensitivities by the Adjoint Variable Method in Nonlinear Structural Dynamics," *SIMS Simulation Conference*, Norwegian Inst. of Science and Technology, Trondheim, Norway, June 1996, pp. 15–21.

[24] Martins, J., Alonso, J., and Reuther, J., "A Coupled-Adjoint Sensitivity Analysis Method for High-Fidelity Aero-Structural Design," *Optimization and Engineering*, Vol. 6, 2005, pp. 33–62. doi:10.1023/B:OPTE.0000048536.47956.62

[25] Rumpfkeil, M., and Zingg, D., "A General Framework for the Optimal Control of Unsteady Flows with Appications," AIAA Aerospace Sciences Meeting, Reno, NV, AIAA Paper 2007-1128, Jan. 2007.

[26] Mavriplis, D., "Solution of the Unsteady Discrete Adjoint for Three-Dimensional Problems on Dynamically Deforming Unstructured Meshes," AIAA Aerospace Sciences Meeting and Exhibit, Reno, NV, AIAA Paper 2008-727, Jan. 2008.

[27] Hall, K., "Eigenanalysis of Unsteady Flows about Airfoils, Cascades, and Wings," AIAA Structures, Structural Dynamics, and Materials Conference, Hilton Head, SC, AIAA Paper 1994-1427, April 1994.

[28] Thomas, J., Hall, K., and Dowell, E., "Discrete Adjoint Approach for Modeling Unsteady Aerodynamic Design Sensitivities," *AIAA Journal*, Vol. 43, No. 9, 2005, pp. 1931–1936. doi:10.2514/1.731

[29] Chittick, I., and Martins, J., "An Asymmetric Suboptimization Approach to Aerostructural Optimization," *Optimization and Engineering*, Vol. 10, No. 1, 2009, pp. 133–152. doi:10.1007/s11081-008-9046-2

[30] Stanford, B., and Ifju, P., "Aeroelastic Topology Optimization of Membrane Structures for Micro Air Vehicles," *Structural and Multidisciplinary Optimization*, Vol. 38, No. 3, 2009, pp. 301–316. doi:10.1007/s00158-008-0292-x

[31] Murthy, D., and Kaza, K., "Application of a Semi-Analytical Technique for Sensitivity Analysis of Unsteady Aerodynamic Computations," AIAA Structures, Structural Dynamics, and Materials Conference, Williamsburg, VA, AIAA Paper 1988-2377, April 1988.

[32] Kolonay, R., Venkayya, V., and Yang, H., "Sensitivity Analysis for Transonic Unsteady Aeroelastic Constraints," *Journal of Aircraft*, Vol. 35, No. 4, 1998, pp. 574–581. doi:10.2514/2.2362

[33] Li, W., and Livne, E., "Analytic Sensitivities and Approximations in Supersonic and Subsonic Wing/Control Surface Unsteady Aerodynamics," *Journal of Aircraft*, Vol. 34, No. 3, 1997, pp. 370–379. doi:10.2514/2.2179

[34] Wilkins, P., and Knowles, K., "The Leading-Edge Vortex and Aerodynamics of Insect-Based Flapping-Wing Micro Air Vehicles," *The Aeronautical Journal*, Vol. 113, No. 1142, 2009, pp. 253–262.

[35] Young, J., and Lai, J., "Oscillation Frequency and Amplitude Effects on the Wake of a Plunging Airfoil," *AIAA Journal*, Vol. 42, No. 10, 2004, pp. 2042–2052. doi:10.2514/1.5070

[36] Neef, M., and Hummel, D., "Euler Solution for a Finite-Span Flapping Wing," *Fixed and Flapping Wing Aerodynamics for Micro Air Vehicle Applications*, edited by T. Mueller, AIAA, Reston, VA, 2002.

[37] Heathcote, S., Wang, Z., and Gursul, I., "Effect of Spanwise Flexibility on Flapping Wing Propulsion," *Journal of Fluids and Structures*, Vol. 24, No. 2, 2008, pp. 183–199. doi:10.1016/j.jfluidstructs.2007.08.003

[38] MATLAB, Software Package, Ver. 2007a, The MathWorks, Inc., Natick, MA, 2007.